# Structural control on fluid circulation in a graben system: Constraints from the Saint Pierre Bois quarry (Vosges, France)

Chrystel Dezayes, Catherine Lerouge, Christophe Innocent, Philippe Lach

Journal of Structural Geology 146 (2021) 104323

Contents lists available at ScienceDirect

Journal of Structural Geology

journal homepage: http://www.elsevier.com/locate/jsg

Review article

# Structural control on fluid circulation in a graben system: Constraints from the Saint Pierre Bois quarry (Vosges, France)

Chrystel Dezayes *, Catherine Lerouge, Christophe Innocent, Philippe Lach

*BRGM, 3, Avenue Claude Guillemin, BP36009, 45060, Orléans Cedex, France*

ARTICLE INFO

*Keywords:*
Fracture
Alteration
Porosity
Sedimentary cover-crystalline basement transition
Riedel shear zone
Rhine graben

ABSTRACT

Defining the fracture network and the active fluid pathways are fundamental to characterizing a fractured reservoir. With this goal, we chose the Saint Pierre Bois quarry (Vosges Massif, France) as a natural analogue for the Permian-Stephanian cover (arkoses)/Hercynian basement (granite) transition that serve as geothermal reservoirs, for example at Rittershoffen, Landau and Insheim, where geothermal plants exploit this kind of reservoir within the Upper Rhine Graben (URG). During our study, along walls of the quarry, we measured fracture orientation on multiple 1D scanlines, sampled fracture fills and associated wall rock, and measured porosity. Our interpretation of the fracture dataset and associated mineral deposits and alteration indicates a large unmapped fault zone (displacement around 10m) we infer to cross the quarry. This fracture zone comprises a core zone (>50 m thick), which is the most highly altered-fractured zone in the quarry. In the transition zone (20–25m thick), some E-W faults cross and displace the arkose/granite transition. The two major fracture sets (E-W and NNE-SSW strikes) are present in the damage zone (>100m thickness) and are typically randomly distributed, but sometimes are grouped in clusters (defined by high spacing coefficient of variation). The E-W fractures and faults are the result of local tectonic inheritance in relation to the Villé basin formation at the end of the Hercynian orogen. Based on rock alteration, these structures constitute good pathways for fluid, first of all for the meteoric fluid during the E-W fault zone creation associated to the Villé basin opening, and then for the hot brine, which clogged the system by quartz precipitation during the burial of the basin.

## 1. Introduction

According to the literature, deep geothermal energy reserves are associated with naturally fractured/faulted reservoirs in various geological contexts (Meixner et al., 2016; Aliyu and Chen, 2018; Torabi et al., 2019). Opening-mode fractures and faults, with associated dilatant parts and damage zones, provide permeability that may constitute flow pathways, especially in low-porosity crystalline rocks, such as in granite (Barton et al., 1995; Caine et al., 1996; Caine and Forster, 1999; Callahan et al., 2019; Hollingworth et al., 2019; and references therein). Fluid flow through faults or fractures is possible due to contrasts in hydraulic conductivity with the surrounding low porosity rock matrix (Gentier et al., 2000). However, the hydraulic conductivity changes with time due to fluid/rock interactions and regional deformation history (e.g. Callahan et al., 2019). Therefore, understanding fracture pattern geometry and its alteration is a major issue in the hydrogeology of fractured reservoirs (Laubach et al., 2019; Gentier et al., 2000).

Fluid-rock interactions lead to chemical changes, mineral dissolution/precipitation and to changes of rock physical properties and strength including fracture growth, shear and linkage, inducing an increasing complexity of the fault zone (Dimmen et al., 2017; Heap et al., 2017; Laubach et al., 2019; Callahan et al., 2020a,b). Field and experimental studies have shown that fluid/rock interactions depend on fluid and rock chemistries and pressure-temperature conditions (e.g. Laubach et al., 2019). The effects of temperature can be marked at shallow (less than 3 km) depths under the elevated heat flow circumstances of hydrothermal conditions (e.g. Callahan et al., 2020a,b; Drüppel et al., 2020; and references therein). Such conditions can lead to either alteration-weakening, favoring by thin clay-rich low-permeability fault cores, or precipitation-strengthening, favored by thick stiff low-permeability fault cores (Solum et al., 2010; Callahan et al., 2020a, b). These effects can vary along individual faults and between faults in a set depending on local geochemical circumstances governed, for example, by host rock composition (Laubach et al., 2014).

In the light of these recent investigations, we examine how fluid-rock

* Corresponding author.
*E-mail address:* c.dezayes@brgm.fr (C. Dezayes).

https://doi.org/10.1016/j.jsg.2021.104323
Received 26 June 2020; Received in revised form 4 March 2021; Accepted 4 March 2021
Available online 18 March 2021

interactions and regional tectonics affected the fracture network architecture and its evolution along the transition between the Hercynian granitic basement and the Permian arkosic cover, which constitute a geothermal reservoir at depth within the Rhine Graben exploited at Rittershoffen (Vidal et al., 2017), Landau (Hettkamp et al., 2013) and Insheim (Baumgärtner et al., 2013).

Our study aims at defining the major parameters that control the efficiency of a fracture network for the flow of geothermally significant fluid, based on an analogue of the deep-seated geothermal reservoir, where we lead:

1) a description of the fracture network including fracture orientation measurements, abundance (density), spatial distribution, microstructures, and deformation style;
2) a mineralization and mineral deposit timing analysis; and

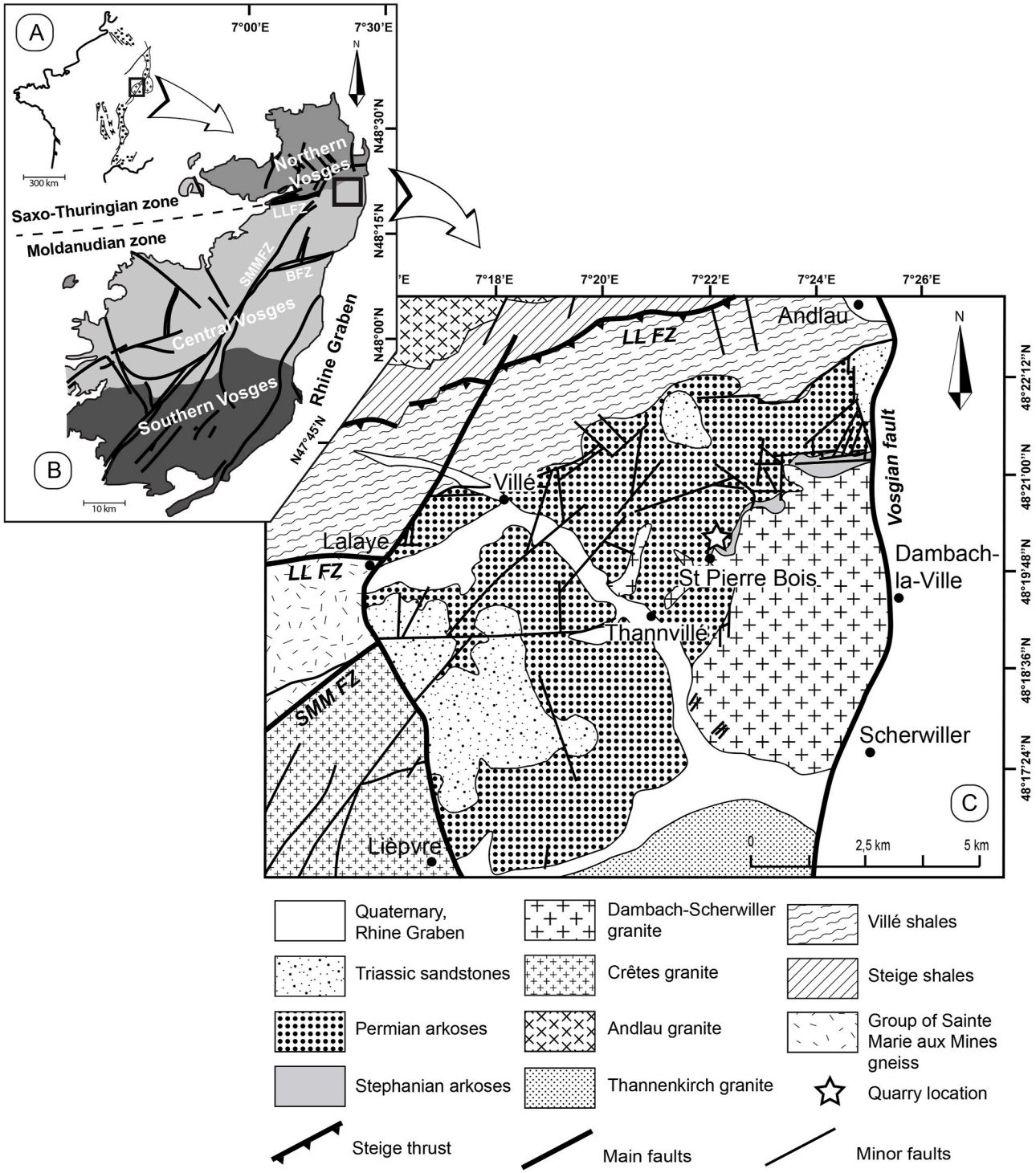


**Fig. 1.** Geological setting of the Saint Pierre Bois quarry area. A- The European Cenozoic Rift System and the location of the Vosges Massif as western shoulder of the rift. B- Simplified map of the Vosges Massif. C- Geological map of the Villé permian Basin (from Blanalt et al., 1972). LL FZ: Lalaye-Lubine fault zone, SMM FZ: Sainte Marie aux Mines fault zone, BFZ:Bilstein Fault Zone.

3) a study of porosity and evidence of fluid/rock interactions at the fracture/fault scale.

Through measuring fractures and characterizing wall rock alteration and mineral fill, we propose a model of the quarry-scale fracture network that integrates fluid circulation related to the geological history. We show that a previously unrecognized fault is present, that constitutes a hydraulic drain, and three stages of circulation have existed within this fault since the beginning of its history.

## 2. Geological setting

### 2.1. Rhine graben context

The Upper Rhine Graben (URG) is part of the European Cenozoic Rift System, which extends from the North Sea to the Mediterranean Sea (Fig. 1-A; Illies, 1972; Ziegler, 1992; Schumacher, 2002; Ziegler and Dèzes, 2005). This extensional structure is bounded by faults that crosscut both Permo-Triassic sandstones and Hercynian basement rocks (Schellschmidt and Clauser, 1996; Pribnow and Schellschmidt, 2000; Baillieux et al., 2013). Tertiary (500–1000 m thick) and Quaternary sediments filling the graben overly Jurassic (about 150m thick) and Triassic (about 700m thick) sediments and the Paleozoic crystalline basement (Rotstein et al., 2006). The URG, which formed after the Eocene in a weakened region, as a result of a thinned crust and an abnormal geothermal gradient, exhibits a vertical downward displacement of approximately 4 km (Illies, 1972; Illies and Greiner, 1978; Ziegler and Dèzes, 2005). Thermal anomalies in the URG are widely interpreted to be the result of large-scale natural convective circulation loops of up to 3 000m height (Le Carlier et al., 1992; Vallier et al., 2019). The Hercynian basement and the Permo-Triassic cover crop out along the eastern and western graben shoulders (Illies, 1972; Walter et al., 2015), which were uplifted as the graben subsided (Schweizer and Kraatz, 1982; Ziegler, 1992).

The Hercynian basement of the URG consists of three major tectonic terranes, trending NE to NNE, and named from north to south: the Rhenohercynian, the Saxothuringian, and the Moldanubian (Fig. 1-B; Edel and Weber, 1995; Ziegler, 1992; Edel and Schulmann, 2009). These terranes crop out in the Vosges Massif and in the Black Forest Massif on the western and the eastern sides of the URG respectively. Successive generations of Carboniferous granitoids were emplaced into these terranes in a NE to NNE direction along primary weakness zones such as collisional or shear zones (Edel and Fluck, 1989). These granitoids exhibit a wide petrological and geochemical diversity, from a variety of deep magmatic sources (Altherr et al., 1999, 2000; Edel and Schulmann, 2009; Skrzypek et al., 2014; Skrzypek, 2016).

The Rhine Graben rifting has produced elevated temperatures (thermal anomalies) that reach temperatures of 100–150 degrees C at depths of as little as 1 km, suitable for economic exploitation of geothermal resources. However thermal anomalies along the graben are spatially restricted (length and width ca. 10 km–30 km) and their intensity varies significantly (90–130 degree C at 1500m depth) throughout the region (Hurter et al., 2003; Freymark et al., 2017). Contrasts between low permeability host rocks and observations of enhance flow in fault rocks shows that this regional heterogeneity is closely related to the capacity of rift-flank faults to support fluid circulation at the crustal scale by hydraulic connections from the crystalline basement to the overlying sedimentary basin (Le Carlier et al., 1992; Cathelineau and Boiron, 2010; Sanjuan et al., 2016).

### 2.2. The Saint Pierre Bois quarry site

In order to understand the Permian cover/Hercynian basement transition as deep geothermal reservoirs, it is essential to use outcrops as analogues (Ukar et al., 2019). In the rift-flanks, in the Vosges and Black Forest massifs, few outcrops allow access to this transition zone. The Saint Pierre Bois quarry is a suitable analogue because it shares the same structural setting and geology of those reached by the boreholes within the Rhine Graben. Additionally, the rocks have mineral deposits and alteration typical of rocks exposed to a hydrothermal activity. Further the three quarry walls provide a 3D picture of the fracture network in both the basement and the overlying sedimentary cover, and of the structural connectivity between them.

The Saint Pierre Bois quarry is located on the western graben shoulder margin, in the Villé basin, in the northern part of the central Vosges (Fig. 1). The Villé basin is bounded by major faults that have more than 100 m of displacements: the Lalaye-Lubine (LL) fault zone to the north (400 m fault throw at the Col de Fourchy, Blanalt et al., 1972), the Sainte-Marie-aux-Mines (SMM) fault zone striking N30°E to the west, and the N–S Vosgian fault to the east (Fig. 1-B). These major faults created a weak crustal domain where the Villé basin (Fig. 1-C) developed during the Permian (Saalian phase) and Triassic and led to basin subsidence in the Miocene during formation of the Rhine graben (Laubacher and von Eller, 1966; Blanalt et al., 1972). The basin hosts a number of secondary smaller horst and graben structures (Blanalt et al., 1972). The Villé Basin was filled with detrital and volcanic-detrital sediments (Laubacher and von Eller, 1966), including Stephanian arkoses and several stages of Permian fluvial filling interrupted by a period of lacustrine sedimentation (Carasco, 1989).

The Saint Pierre Bois quarry, currently exploited for aggregate, is located more precisely along the border of the Dambach-Scherwiller granite, which constitutes a horst within the Villé basin (Fig. 1-C). This granite is related to the generation of S-type two mica leucogranites ('Thannenkirch-Brézouard-Bilstein') that were emplaced as an elongated pluton along major crustal faults during the late Carboniferous magmatic event in the Central Vosges (Skrzypek et al., 2014; Skrzypek, 2016). These magmatic plutons were intruded 322–330 Ma ago (Boutin et al., 1995; Schulmann et al., 2002; Edel et al., 2007; Kratinová et al., 2007; Tabaud et al., 2014). In the quarry, a layer of Stephanian arkose including granite clasts overlies the Hercynian granite. The arkose layer thickness does not exceed 15 m within the Villé basin (Laubacher and von Eller, 1966) and is 1–5 m in the quarry (Fig. 2-B).

## 3. Methodology

### 3.1. Fracture network parameters

In the whole paper, the term *fracture* groups opening-mode fractures and faults in general and particularly if we cannot distinguish a displacement. We use the term fault if we showed a displacement along the surface.

The spatial arrangement of a fracture network is a fundamental attribute to characterize (Laubach et al., 2018). Spatial arrangement includes the spacing patterns of fractures (e.g. random, regularly spaced, clustered) and the configuration of the parts of the network (size, strike dispersion, and connectivity). The distribution of fracture orientations (strike and dip) and connectivity (abutment, cross-cut, and type of termination) influences connected flow pathways (Long and Witherspoon, 1985) if the fractures are open.

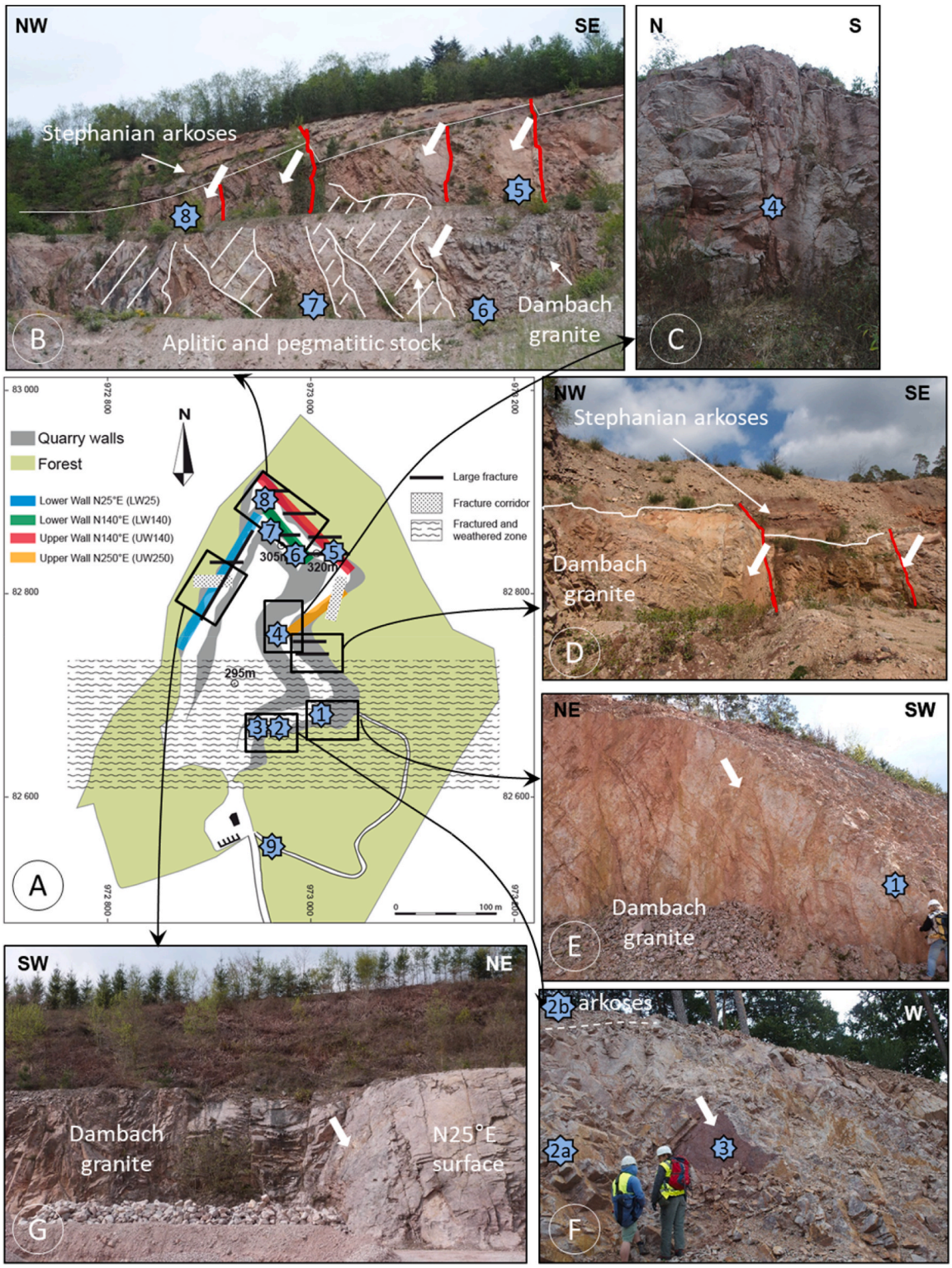


**Fig. 2.** A- Schematic map of the Saint Pierre Bois quarry. Altitudes are measured above sea level (ASL). B- The N140°E walls (UW140 and LW140) showing large E-W fracture planes crosscutting leucogranite intruded by a stock of aplites and pegmatites. Most stop at the basement/cover transition, although some cross the interface. C- The N250°E wall (UW250) showing a fracture corridor. D- Transition between basement and sedimentary cover showing E-W fault crossing the interface and having a normal movement. E– Large E-W bleached fault. F- Highly fractured and altered zone. G- The N25°E wall (UW25) showing E-W fault reworking N25°E fault surface. Wall heights are around 10 m. White arrows indicate E-W faults. Numbered blue stars show sample sites for petrological and geochemical study. Sample 1 is located in a E-W fault. Sample 2a and 2b were taken in the blasted granite and arkose respectively. Sample 3 is located in a E-W dextral fault with iron hydroxide fill. Sample 4 is located in a E-W corridos. Sample 5 and 6 are located in a E-W fault crossing the arkose/granite transition and showing macroscopic breccia. Sample 7 and 8 were taken out of fracture in the granite. (For interpretation of the references to color in this figure legend, the reader is referred to the Web version of this article.)

Additionally, other key fracture parameters needed to understand likely flow pathways include fracture abundance in terms of size and number, population of apertures (dilations, fill), and mineral fill composition, distribution, and timing. The degree to which fractures become sealed depends on a number of factors including temperature conditions, geochemical environment, fluid flow patterns, fracture size, and when and how fast fractures opened (Laubach et al., 2019 and references therein).

To characterize arrangement, we used the scanline method (Priest and Hudson, 1981; Sanderson and Peacock, 2019). For each fracture, we measured orientation and position of the fracture intersection with the line, aperture and fill geometry and composition.

Fracture orientations for each scanline were plotted in rose diagrams and equal-area, lower-hemisphere stereonets to identify orientation modes that were used to define fracture sets. Having the orientation of a scanline, the set orientations, and the position of scanline intersections for each set, the spacing between fractures of each set has been adjusted by applying the Terzaghi correction (Terzaghi, 1965) (1).

$$S_c = S_m * \sin \alpha \quad (1)$$

Where $S_c$ is the corrected spacing, $S_m$ is the measured spacing, and α is the acute angle between the scanline and the average orientation of the fracture set.

For each set, stick plots and cumulative frequency diagrams were used to analyze spatial distribution (Gillespie et al., 1999; Sanderson et al., 2019). Moreover, to quantify fracture distribution along the scanline, a coefficient of variation Cv was computed. This coefficient corresponds to a dimensionless value of spacing variation (Gillespie et al., 1999) (2).

$$C_V = \frac{\sigma_S}{S} \quad (2)$$

where $C_V$, $\sigma_S$, $S$ are coefficient of variation, standard deviation of spacing between fractures, and mean spacing, respectively. This value provides an indication of the fracture distribution: $C_V < 1$ indicates regularly spaced fractures whereas a $C_V > 1$ is characteristic of fractures that are more irregularly spaced and Cv = 1 expected for random distribution (Sanderson et al., 2019) and perhaps clustered (Gillespie et al., 1993).

Fractures that are anomalously closely spaced have been called corridors (e.g. Questiaux et al., 2010). Random spacing can result in clustering. We identified corridors qualitatively and by using high Cv values although we note that methods exist that can separate patterns where clustering is more pronounced than random patterns and those that are not (Marrett et al., 2018; Wang et al., 2019).

### 3.2. Petrological characterization

Petrological characterization of rock samples was undertaken based on polished thin section analyses using a combination of optical and scanning electron microscopy. An Olympus BH2 polarising light microscope was used to observe thin sections. A Tescan Mira 3 XMU scanning electron microscope (SEM) coupled with an EDS EDAX TEAM system and an APOLLO XPP silicon drift detector at 25 kV, was used for further investigations at high magnification.

Chemical spot analyses of silicates were performed using an electron microprobe with an accelerating voltage of 15 kV, a beam current of 12 nA, a 1 μm beam width and a counting time of 10 s. Ca, K, Na, Mg, Si, Al, S and Fe were analyzed. Ca-Ka and K-Ka were monitored with a LPET crystal, Na-Ka and Mg-Ka on a LTAP crystal, Si-Ka and Al- Ka on a TAP crystal, S-Ka on a PET crystal, Fe-Ka on a LLiF crystal. Chemical spot analyses of alumino-phosphate-sulfates were performed using electron microprobe with an accelerating voltage of 20 kV, a beam current of 40 nA, a 1 μm beam width and a counting time of 10 s. Na, Mg, Al, Si, P, S, K, Fe, Mn, Zr, La, Ce, Th, U, Ba, Sr and As were analyzed. Standards included both well characterized natural minerals and synthetic oxides. Matrix corrections were made with the ZAF software program (Merlet, 1994).

### 3.3. Porosity measurements

In the present work, four techniques were applied to different sample types to provide porosity data in the fracture network and granite wall rock. The triple-weighing method was used to measure the porosity of interconnected pores (intergranular and fracture porosity) for large samples (up to 3.5 kg) along and in corridors. This method consists of drying the sample under vacuum at 105 °C, saturating the sample with water under vacuum, and weighing both the dry and saturated samples in air and submerged in water.

Prior to analysis, vacuum or flow degassing removed moisture from the porous rock. To establish the relationship between texture and porosity, helium pycnometry was applied to small sub-samples of the large samples collected from corridors. Helium pycnometry measures the true bulk density, because helium can enter even the smallest voids or pores. Mercury porosimetry was used to measure pore volume, pore size distribution, and bulk and apparent densities. During porosity analysis in the mercury porosimetry analyser, increasing pressure was applied to forcefully intrude mercury into the smallest pores. Pore size distributions ranging from 4 nm (pressure = 400 MPa) up to ~ 800 μm (vacuum) can be measured.

Digital image processing applied to back-scattered electron (BSE) images obtained with scanning electron microscopy was used to quantify total porosity and feldspar dissolution porosity, to measure pore size distribution, and to complement the other techniques with textural and spatial information about porosity (Cardell et al., 2002). Total porosity corresponds to an average value of ten porosity measurements on ten separated low-magnification BSE images (9 × 7 mm), using the Image J software (Rotevatn et al., 2016). Feldspar dissolution porosity was estimated by measuring porosity on most of the feldspar grains observed in five high magnification images (1.36× 1.02 mm). Taking account of the feldspar grain size, the number of grains measured in thin section is around 20.

### 3.4. Geochemistry

#### 3.4.1. Trace elements in quartz

Analyses of trace elements in quartz were performed using a UVl laser-ablation microsampler CETAC® Excite (193 nm) coupled to a ThermoScientific® X series II quadrupole plasma mass spectrometer at the BRGM laboratory in Orleans, according to the laser configuration of Monnier et al. (2018). The analytical protocol involved combinations of: $^{7}$Li, $^{23}$Na, $^{24}$Mg, $^{27}$Al, $^{29}$Si, $^{39}$K, $^{45}$Sc, $^{48}$Ti, $^{51}$V, $^{52}$Cr, $^{56}$Fe, $^{74}$Ge, $^{75}$As, $^{85}$Rb, $^{93}$Nb, $^{118}$Sn, $^{121}$Sb, $^{139}$La, $^{175}$Lu, $^{181}$Ta, 182W, $^{208}$Pb. Ablation spots 85 μm in diameter were performed at 8 Hz frequency with energy of ~2 J/cm$^2$. Analysis time for each spot was 60 s, including 20 s of background measurement with the laser off and 40 s of analysis time with the laser on. Quantification was performed with Glitter® software. All data were calibrated against the external standard NIST SRM 612, and the internal standard of the Si value (4.65 × 105 ppm = stoichiometric concentration of Si in quartz). Absolute concentrations were calculated

in quartz samples using NIST concentration values given in Pearce et al. (1997).

#### 3.4.2. U–Th measurements

Iron hydroxides analyzed for U–Th were dissolved in a HCl 6N–$HNO_3$ 7N mixture. U and Th were measured on a Neptune MC-ICP-MS equipped with a RPQ filter. The $^{232}$Th isotope was measured using a Faraday cage, whereas $^{230}$Th was measured on an ion counter. The measured values were corrected with certified standards. Blanks are 10 pg for U and 300 pg for Th. Further details on analytical techniques are available in Innocent et al. (2005) and Millot et al. (2011).

## 4. Results

### 4.1. Description of the quarry and fractures observed

The Saint Pierre Bois quarry covers a surface area of around 5 ha with a 40 m-high wall providing access to two around 15 m-high operating levels (305 m and 320 m ASL) on the north side and a large operating platform (level 295 m ASL) on the east (Fig. 2-A). Level 320 m currently has a N140°E wall at the north, called upper wall N140°E (UW140), which is extended by a N250°E wall, called upper wall N250°E (UW250). Level 305 m has a N140°E wall at the north, called lower wall N140°E (LW140), which continues as a N25°E wall along the northwest, called lower wall N25°E (LW25).

On UW140, LW140 (Fig. 2-B) and UW250 (Fig. 2-C), the Dambach leucogranite occurs as a coarse-grained pink to reddish and stiff granite. A stockwork of decameter-to meter-thick pink aplite and pegmatite intruded the leucogranite, largely visible on UW140 and LW140 (Fig. 2-B). Around 5 m of Stephanian sediments, including microconglomerates and arkoses, cover the leucogranite on the western part of the UW140 (Fig. 2-B).

The quarry rocks are not all equally altered and alteration of granite is marked by color changes. On LW25, the leucogranite has lost its pristine magmatic coarse-grained texture due to alteration and its color evolved from pink-reddish in fresh rock to whitish/yellowish color in altered rock (Fig. 2-G). At the south of UW250, active quarrying in 2012 progressively revealed an intensely fractured and yellowish/whitish altered leucogranite overlain by altered Stephanian sediments (Fig. 2-D, E, F).

The granitic basement is highly fractured. It is not always too easy to distinguish pre-existing naturally occurring fractures from those induced by blasting during the quarrying. We call the naturally occurring features ‘tectonic fractures’ in that they are either faults or are primarily associated with faults. The blast fractures are short (less than 1 m), totally scattered (wide orientation dispersion), generally located inside the blocks delineated by tectonic fractures, and do not show any displacement or fill. In contrast, tectonic fractures in the granite have cataclastic textures on their walls, hydrothermal alteration and/or mineral deposits. No opening has been observed on these fractures. Faults are also observed among fractures. The displacement size of faults is challenging to measure in the generally featureless granitic rocks. For the larger ones that cross the sediment-basement transition, we estimated offsets based on the displacement of the arkose layer.

A dozen of E-W opening-mode fractures and small-displacement faults having trace lengths of several meters or more are present along both levels UW140 and LW140. These fractures appear to be regularly spaced (Fig. 2-B). Most of the E-W fractures that crosscut the granite terminate at the sedimentary cover, but several (around 20 percent) cross the interface and some of them (around 20 percent) are faults that show normal (around 1 m; Fig. 2-B and D) or shear (slickensides) displacement. On the E-W-striking faults, only five present slickensides. Plunges are 15°–40° to the west. Based on local crystallization in irregularities, all show dextral move. Evidence of dextral strike-slip movement sense has also been observed on three N130°E fault surfaces. Only one N15°E plane shows evidence of sinistral movement.

Except for the E-W faults, which cross between quarry walls and therefore have map-view trace lengths of at least 20 m, fracture length is challenging to measure accurately. Based on limited trace length exposures, we infer that most have lengths of less than 10m.

Zones of anomalously closely spaced fractures (corridors) are dispersed throughout the quarry. Spacing outside corridors is typically 10–50 m. Spacing within corridors ranges from 5 cm to 3 m. On UW250, a 2–3m thick fracture corridor with high density (spacing 1–5 cm) of N15°E parallel fracture is present at the beginning of the scanline (Fig. 2-C). The granite shows cataclastic textures. This type of corridor is also present in other places in the quarry, but these corridors are narrower, typically only about 5–10 cm thick.

Mineral deposits associated with fractures and faults vary along their traces. Reddish and green coatings are present on most of the fault surfaces (>90%). Centimetric barite and quartz deposits have been only observed on a same E-W fault crossing UW140 and LW140 (Fig. 2-B). On LW25, an E-W fault with compact breccia of cm-sized clasts in a cataclastic matrix separates two blocks with a several-meters offset (Fig. 2-G). At the north-east, E-W faults also cross a N25°E fault surface, and slightly offset the different blocks (<1 m). This N25°E surface constitutes a large fracture in the same direction as the N25°E-striking quarry wall. The fault facilitates quarrying. The fault is also present above at the quarry floor (295 m ASL), where iron oxides and hydroxides are present on the fault surface.

### 4.2. Fracture network in granite

#### 4.2.1. Fracture orientations

Two main sets of fractures in granite have been identified. F1 strikes N90°E±20° and most fractures are nearly vertical. F2 strikes N30°E±20° and dips 55° to SE (Fig. 3-E). The relative ages of the two sets based on crossing and abutting relations is F1 before F2.

Although two-dimensional maps have many advantages for fracture pattern characterization (e.g. Rauch et al., 2019), the configuration of our quarry exposure mandated 1D scanline measurements. Sampling bias, such as undersampling due to being less perpendicular and more parallel to the line, can be minimized for scanlines by collecting multiple measurements in different orientations (Pickering et al., 1995; Davy et al., 2006; Bertrand et al., 2018).

Therefore, we performed several scanline analyses along two perpendicular directions, NE-SW and NW-SE, on the four accessible quarry walls: UW140, UW250, LW25, LW140 (Fig. 2-A). The two NW-SE scanlines (UW140 and LW140) are located at different levels, making it possible to estimate the vertical extent of the fractures.

A total of 229 fracture orientations were measured (Table 1). On the N25°E and N140°E walls (LW25, LW140 and UW140), the most abundant fracture set is oriented N90°E±10° dipping steeply (60–90°) north and south (Fig. 3 A, B, C; F1 in Table 1). On LW25, the dips are equally distributed to north and south, whereas on LW140 and UW140 most fractures dip to the south. A second set, oriented N20°E-N40°E is present, dipping approximately 55° to the SE (Fig. 3 A, B, C; F2 in Table 1). On UW250, the main fracture set is oriented N10°E-N20°E. The E-W set

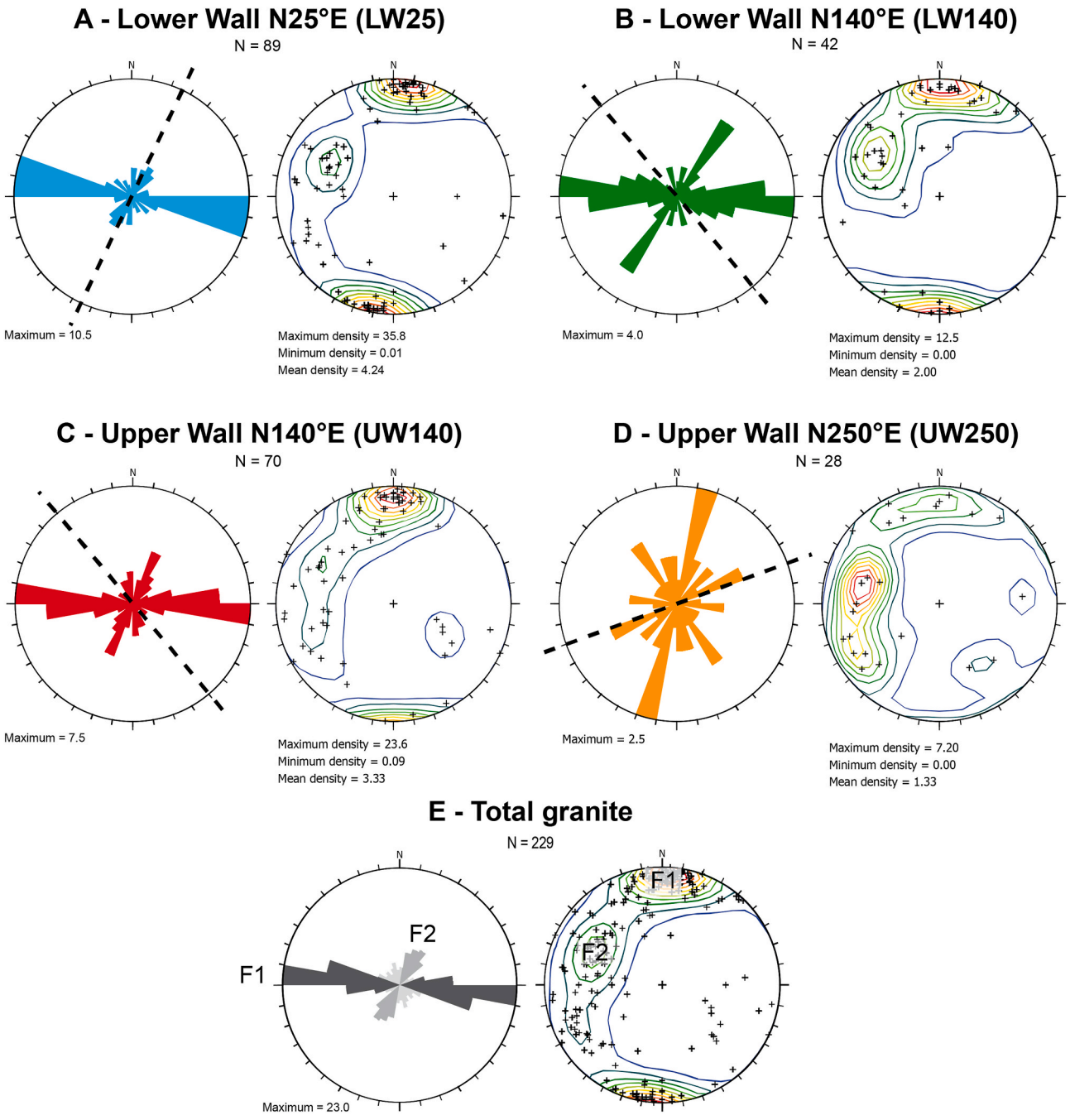


**Fig. 3.** Fracture orientation measured in Hercynian granite on each wall of the quarry (A to D) and total fractures in granite (E). For each figure, N: number of data, left: symmetrical rose diagram of direction (10° classes, radius corresponds to 100% of the maximum class), right: crosses are projections of fracture poles, contour density of fracture pole (10° intervals). Schmidt diagram; equal area projection; lower hemisphere. N: Number of fracture data. Black dashed line represents the direction of the scanline.

**Table 1**
Fracture number, mean frequency and spacing, and Cv value by set by scanline. Length: total length of each scanline.

| Walls | Scanline | Number of fracture | | | | Mean frequency ($m^{-1}$) | Mean spacing (m)[a] | | Cv of spacing[a] | | Fracture distribution | |
|---|---|---|---|---|---|---|---|---|---|---|---|---|
| | Length (m) | All | F1 | F2 | F3 | All | F1 | F2 | F1 | F2 | F1 | F2 |
| LW25 | 135 | 89 | 48 | 19 | 19 | 0,66 | 2,19 | 0,40 | 0,84 | 1,35 | Random | Clustered |
| LW140 | 54,3 | 42 | 24 | 13 | 5 | 0,77 | 1,81 | 3,91 | 1,21 | 0,78 | Random | Random |
| UW140 | 111,4 | 70 | 35 | 19 | 16 | 0,63 | 3,11 | 5,74 | 1,90 | 1,26 | Clustered | Random |
| UW250 | 26 | 28 | 5 | 9 | 14 | 1,08 | 2,36 | 1,24 | 0,58 | 2,35 | Regular | Clustered |
| **TOTAL** | **326,7** | **229** | **112** | **60** | **54** | | | | | | | |

[a] With Terghazi correction.

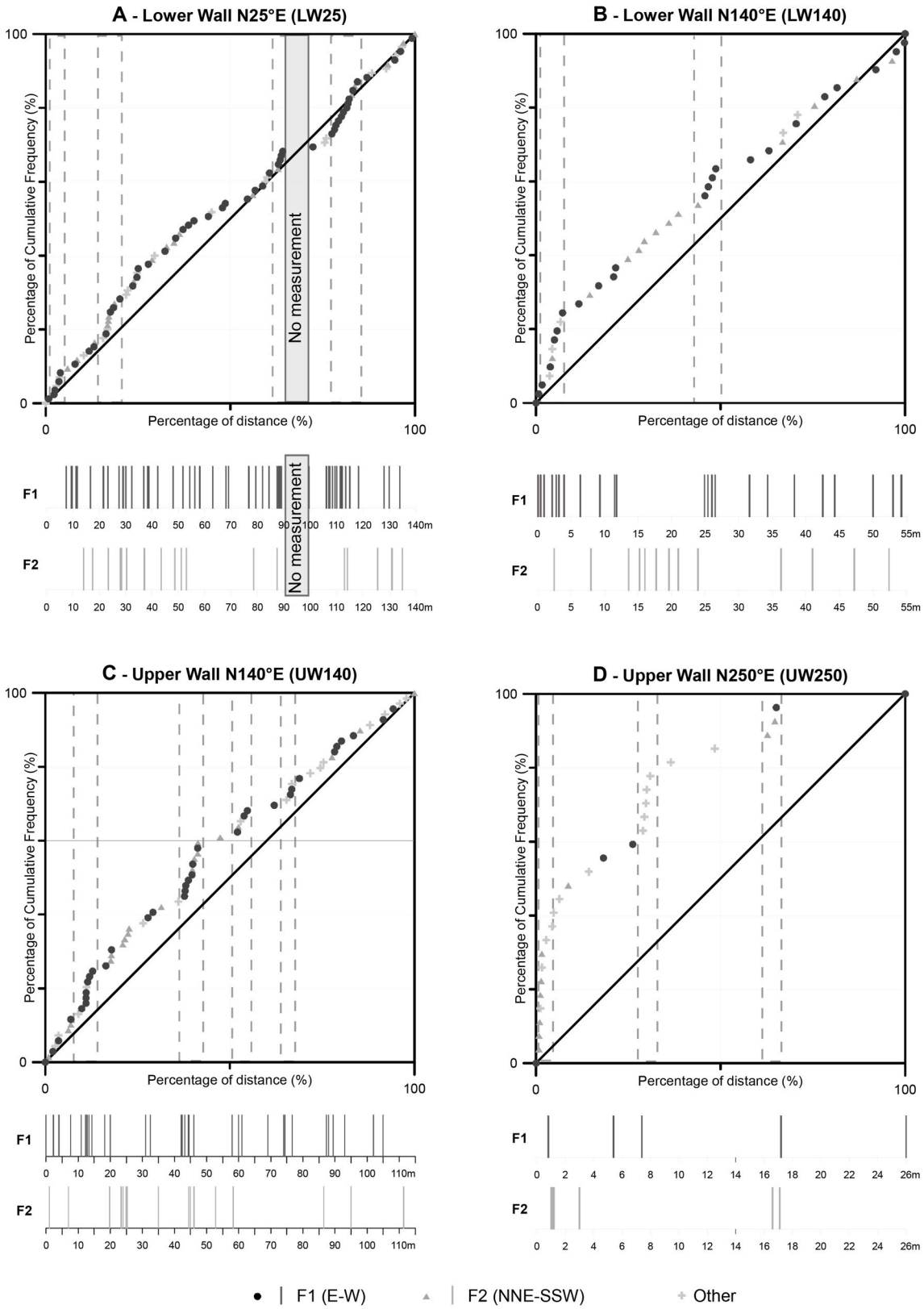


**Fig. 4.** Fracture distribution along each scanline. Cumulative plot of frequency percentage against distance percentage. The diagonal represents uniform distribution. The stick plot shows the position of the fracture along the scanline. Dashed contoured bands indicate rapid increase of fracture number (slope threshold $> 2$).

is also present but is less presented due to the high fracture density within the fracture corridor (Fig. 2-C).

For all scanline directions, the fracture patterns are equivalent in terms of orientation (share common strike), whereas the density of each set varies. This suggests that our sampling is appropriate and spacing is not distorted by sampling bias.

#### 4.2.2. Spatial distribution

Spatial analysis is summarized in Table 1. Fracture frequency is approximately 0.7 ± 0.07 fr/m, except for the UW250 scanline, which shows a higher fracture frequency, approximately 1 fr/m.

Ideally, spacing between two parallel fractures should be measured perpendicular to fracture orientation. To correct spacing values for non-orthogonal fractures, the Terzagi correction has been applied (Table 1). For F1, the mean corrected spacing is 2.5 ± 0.6m. The mean spacing of F2 is more scattered and varies between 0.4m and 5.74m. The lowest value can be explain by the low angle between the average direction of the fracture set (N30°E) and the scanline direction (N25°E). In this case, the scanline direction is not favorable to sample the F2 fractures.

The coefficient of variation (Cv) is around 1 except for F1 along UW140 and F2 along UW250. To better discriminate fracture organization, we used the 95% confidence interval of Cv values for random arrangements based on Monte Carlo simulations (Hooker et al., 2018). Following this approach, the F1 set shows a random arrangement along LW25 and LW140, the lower wall, a clustered arrangement along UW140, and a regular arrangement along UW250 (Table 1). In contrast, fractures of F2 set are randomly spaced along LW140 and UW140, and clustered along LW25 and UW250 (Table 1).

Fracture distributions are presented in Fig. 4. Examining the LW25 scanline from left to right shows regular fracture distribution at the beginning, then increased frequency (a cluster), followed by a regular distribution (Fig. 4-A). Four intervals have a slope higher than 2 and indicate fracture clusters (Fig. 4-A). The two first clusters, around 10m and 30m, are made up of fractures from both sets, whereas the other two, around 90m and 110–120m, are mainly defined by fractures of the F1 set. (Fig. 4-A).

Along the LW140 scanline, a high fracture density zone is present at the beginning of the profile and in the central part, around 25m, mainly made up of fractures of the F1 set (Fig. 4-B). Between these fracture clusters, the fracture distribution is regular, but large intervals have no fractures of the F1 and F2 sets, between 12m and 25m and 25m and 35m respectively (Fig. 4-B). These intervals correspond to the stockwork of aplite and pegmatite intruded into the Dambach leucogranite.

Four fracture clusters are also present in the UW140 scanline around 15m, 45m, 60m and 75m, which correspond to an increase of the number of fractures included mainly in the F1 fracture set (Fig. 4-C).

Along the UW250 scanline, the shortest, three fracture clusters are clearly visible at the beginning of the scanline, around 8m and 17m respectively (Fig. 4-D). The first and the third clusters are mainly constituted of F2 fractures and the second cluster by fractures not included in the F1 and F2 sets.

Along the UW140, the E-W traces are easy to detect. Trace spacing is regular and the analysis of their distribution shows an average spacing of approximately 11m. The Cv is 0.34, which confirms the regular distribution of these large E-W faults, which cross all the walls in the quarry (Fig. 2-B).

#### 4.2.3. Fracture fill and wall rock alteration

The least altered and deformed granite present on UW140 and LW140 that can be considered as a reference for the Dambach granite, is coarse-grained pink to reddish and stiff. It consists of quartz (~40 wt%), K-feldspar (~25–30 wt%), plagioclase (~25–30 wt%) with biotite and muscovite. Primary K-feldspar, plagioclase and muscovite are typically preserved (>95%) Less than 5% of K-feldspar grains and plagioclase core grains are slightly altered into illite-mica. Plagioclase rims consist of albite that shows a green color in cathodoluminescence. Less than 20% of flakes of brown biotite remain well preserved, other flakes show greenish rims with hematite. Less than 1% of flakes are altered to clay minerals (illite) with titanium oxides and iron hydroxides.

The granite samples 7 and 8 taken out of the faults on the UW140 and LW140 are fractured and brecciated (Fig. 2-A, B). In sample 7, millimeter-to cm-sized blocks of microfractured and deformed granite are separated by heterogeneously crushed granite, indicating a proto-cataclastic texture. Biotite and feldspars are slightly altered (<5%) in the largest blocks, while in the crushed granite, biotite is transformed to illite-smectite mixed layers and iron hydroxides, or chlorite, illite and hematite, plagioclase are replaced by illite and K-feldspar is partially dissolved and cemented by quartz. In sample 8, a 1 cm-thick cohesive cataclasite is in contact with a zone of heterogeneous brittle deformation (Fig. 5-a, b, c) that transitions between cataclasite (Fig. 5-c), proto-cataclasite (Fig. 5-d), and altered granite (Fig. 5-e). The cohesive cataclasite is made of <50 μm-sized mineral clasts (essentially quartz (>95%) with minor preserved K-feldspar and plagioclase) cemented by silica/microquartz and minor illite (Fig. 5-c).

In contrast granite samples in the eastern part of the quarry have a whitish/yellowish aspect due to advanced alteration of biotite and feldspars (Fig. 2-A, D, E, F). Biotite is generally altered to clay minerals (illite-smectite mixed layers) with titanium oxides (>99%), while plagioclase grains are intensely altered into clays (kaolinite/illite-smectite mixed layers) and impregnated with iron hydroxides, and feldspar grains are altered into clay mineral.

*4.2.3.1. Fault rocks.* To document mineral deposits and textures in EW-striking fractures, six samples were collected (Fig. 2-A).

The coating of sample 1 is a 2-3 cm-thick cohesive cataclasite intersected in its length by a ~0.5 mm-thick opening-mode fracture (Fig. 6-a, b). The cement of cohesive cataclasite is silica/microquartz with minor illite. The opening-mode fracture is lined by inward-facing euhedral quartz and sealed by anhedral barite (Fig. 6-b, d). Quartz grains are ~100 μm-sized. The cohesive cataclasite is in contact with altered granite matrix affected by a low-density network of micro-fractures subparallel to the cataclasite. Microfractures are filled with radial fibers of iron-hydroxides sealed by microquartz with minor illite (Fig. 6-g). Biotite has altered to illite with titanium oxides and hematite (Fig. 6-c). K-feldspar and plagioclase grains are partially dissolved (Fig. 6-e). Quartz partially fills K-feldspar porosity, while illite and μm-sized aluminum-phosphate-sulfate (APS) minerals fill plagioclase porosity (Fig. 6-f).

The coating of sample 2a is a 4-5 cm-thick cohesive cataclasite in contact with a highly deformed and altered granite (Fig. 6-h). A ~1 cm-thick opening-mode fracture intersects the cohesive cataclasite in its length (Fig. 6-j). The opening-mode fracture is lined by well-crystallized hematite and euhedral quartz, and sealed by anhedral barite (Fig. 6-j). The altered granite is formed of micro-domains of folded quartz and clasts of identifiable granite separated by microfractures sub-parallel to the cataclasite (Fig. 6-h). The microfractures are sealed by microquartz and iron hydroxides. In granite clasts, clay minerals (illite-smectite mixed layers) and iron-hydroxides replace deformed flakes of biotite (Fig. 6-i). K-feldspar and plagioclase grains are intensely dissolved and replaced by clay minerals.

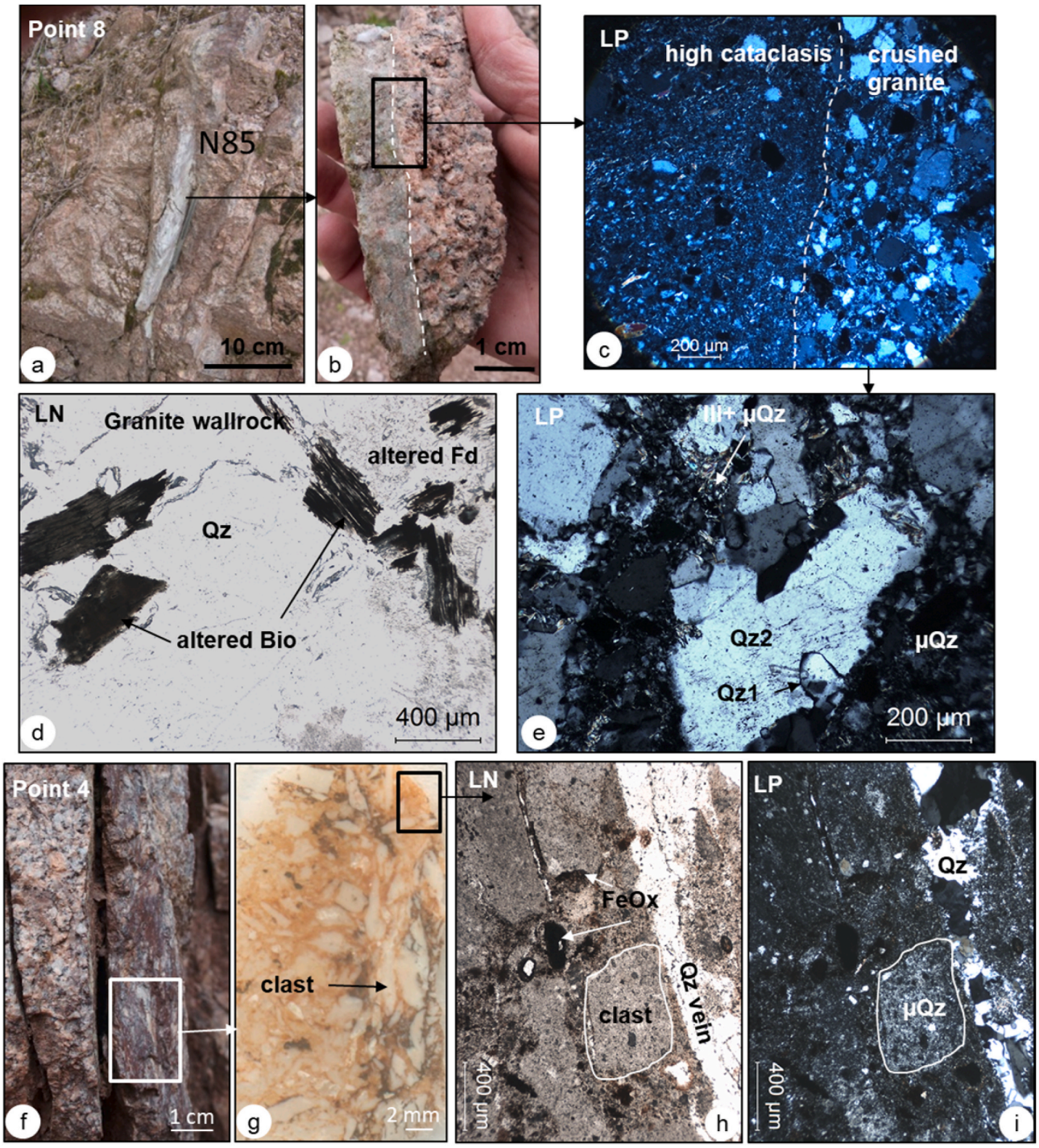


**Fig. 5.** Cataclasite from samples 4 and 8 (see location Fig. 2). Sample 8: (a) whitish cataclasite in place; (b) cm-thick cataclasite; (c) micrograph in polarized light showing the contrast between cataclasite on the left and protocataclasite of the granite; (d) altered granite of the wall rock (transmitted light); (e) protocataclasite cemented by illite and microquartz, and late medium-quartz (Qz1 and Qz2) (polarized light). Sample from corridor: (f) reddish aspect of fractured granite on the outcrop; (g) polished section of a breccia cm-sized corridor; (h) quartz veinlet crosscutting the breccia (transmitted light); (i) same picture in polarized light showing that clasts consist of microquartz, and clasts are also cemented by microquartz.

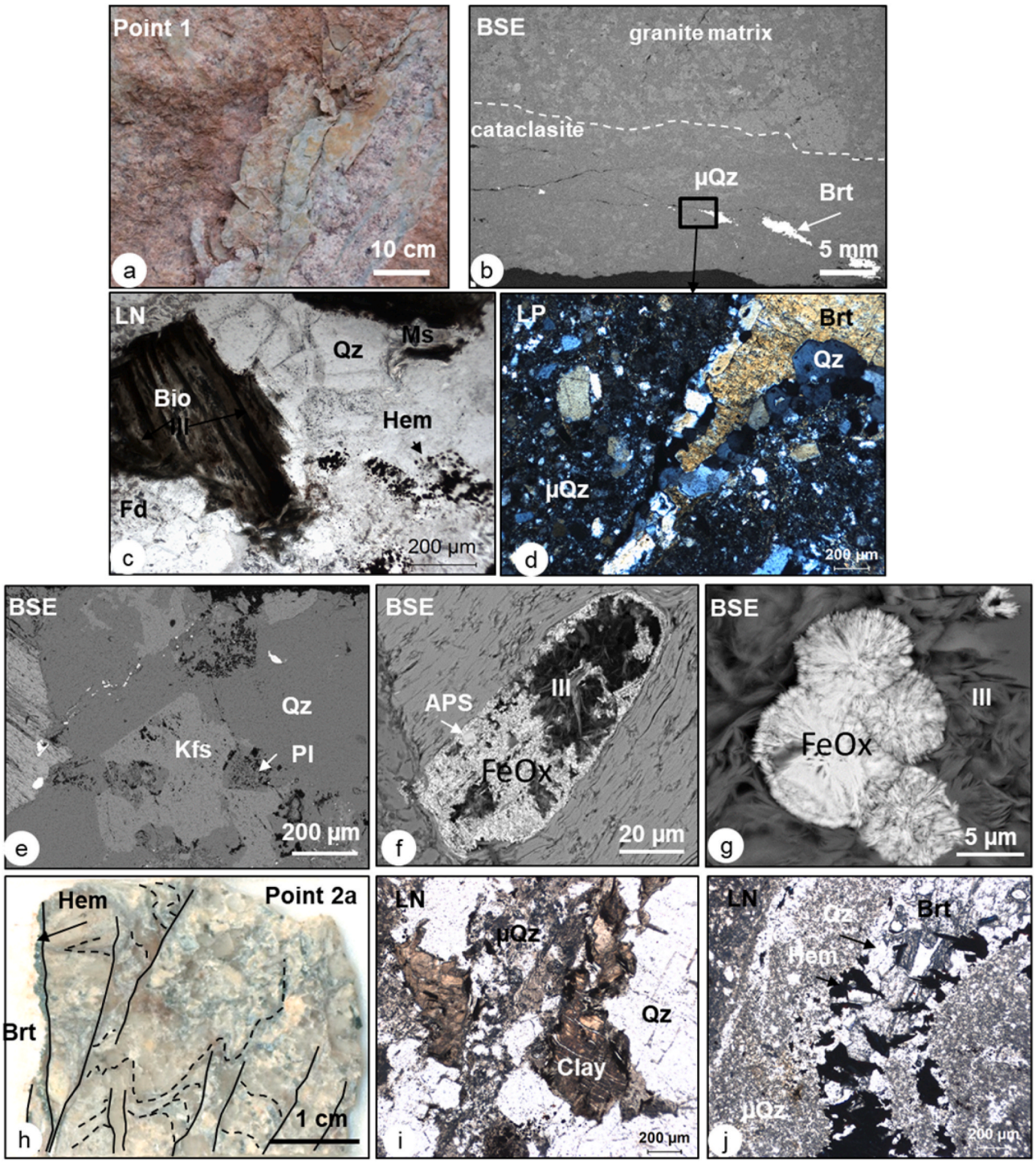


**Fig. 6.** Breccia samples 1 and 2a from the altered-fractured zone in the eastern part of the quarry. Sample 1: (a) outcrop; (b) back-scattered electron (BSE) image of thin section showing the contact between cataclasite and granite matrix, and late generation barite crosscutting cataclasite; (c) alteration of granite matrix (transmitted light); (d) euhedral quartz and barite crosscutting the cataclasite (polarized light); (e) BSE image showing the different intensities of feldspar alteration in the granite matrix; (f) BSE image of a phantom mineral replaced by illite, APS and iron hydroxides (FeOx); (g) Radial fibrous iron hydroxides formed in residual porosity of plagioclase dissolution. Sample 2a: (h) polished section of breccia showing ductile-brittle deformation of granite matrix crosscut by quartz-hematite-barite vein on the left; (i) highly altered granite matrix (transmitted light); (j) cataclasite corridor crosscut by quartz-hematite-barite vein (transmitted light).

The coating of sample 3 is a 2-3 cm-thick almost friable cataclasite of granite cemented by iron-hydroxides with minor microquartz. The alteration of the granite matrix is very similar to that of granite clasts in sample 2.

The breccia of sample 4 consists of mm-sized clasts of microbreccia/cataclasite cemented by microquartz with iron hydroxides and minor illite (Fig. 5-f, g, h, i). A medium-sized quartz fills residual porosity and microfractures that intersect the breccia in its length (Fig. 5-i). No preserved granite matrix was observed at this site.

The breccia of samples 5 and 6 essentially consist of clasts of granite, mineral grains and cataclasite that are partially cemented by microquartz with minor iron hydroxides and illite, then euhedral quartz and barite (Fig. 7-a, b, c, d). The size of clasts varies widely, from several centimeters to a micron. In the two samples, a part of the porosity is related to two sets of opening-mode fractures (Fig. 7-c). Microfractures sub-parallel to fractures crosscut the minerals especially the longest ones, while the smallest ones follow intergrain boundaries. Some microfractures are not continuous but extend as planes of secondary fluid inclusions that are easily visible in deformed primary quartz. Mineral fillings in microfractures are similar to those present in cataclasite and breccia, i.e. essentially quartz with minor clay minerals and iron hydroxides. However, at the micron scale, it is difficult to distinguish the quartz cement from micron-sized quartz clasts. Euhedral quartz partially deposited on the walls of residual macroporosity, while late millimetric to centimetric barite only seals up part of the porosity at intersections of fractures with almost the same direction but various dip. In the sample 6, an early 2 cm-thick cohesive cataclasite shows two zones: 1) a reddish one that is essentially cemented by iron hydroxides with minor microquartz and 2) an indurated orange one cemented by silica/microquartz (Fig. 7-a, f, g). Residual macroporosity along cataclasite partially filled with euhedral quartz forms mm-to cm-sized geodes.

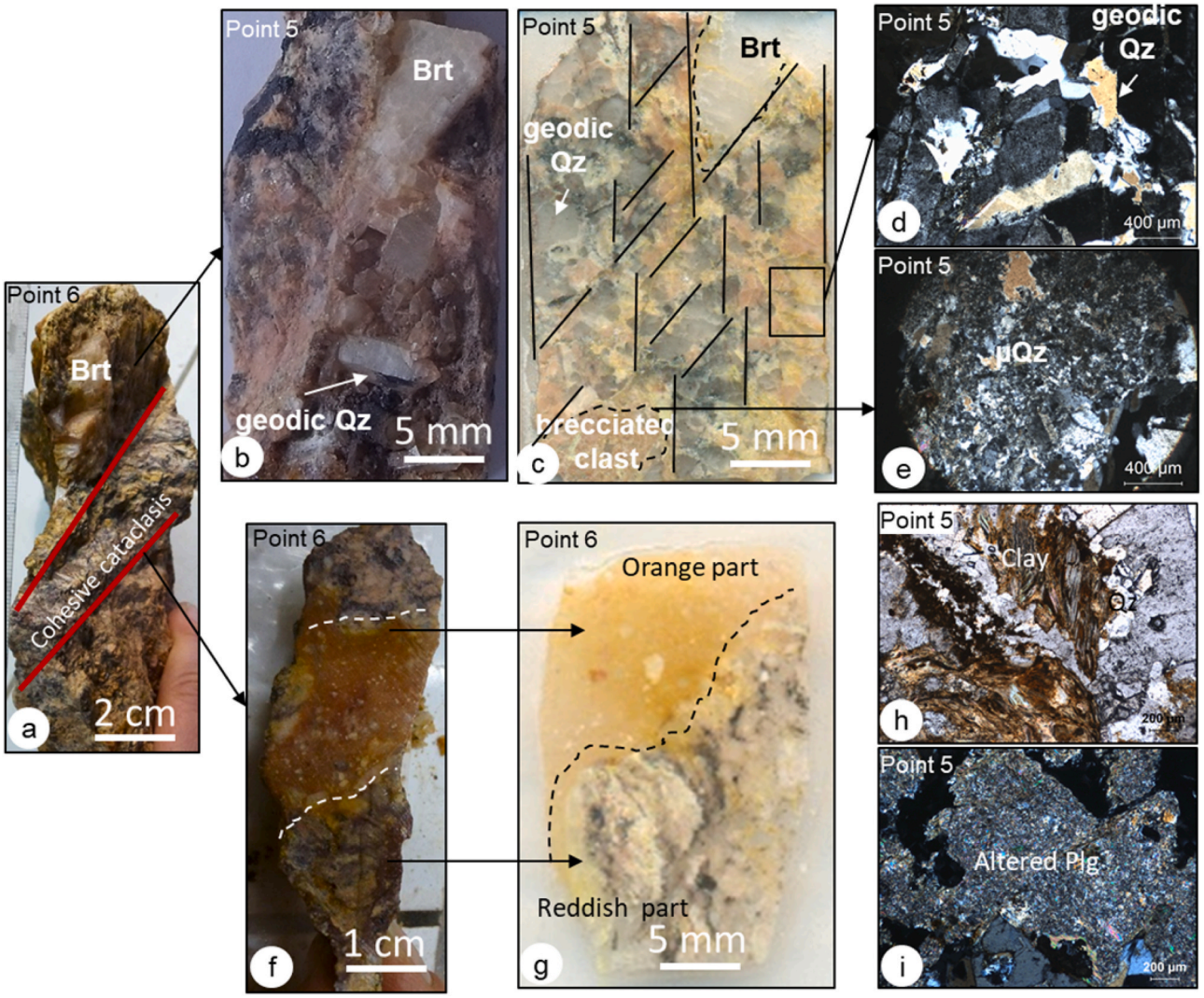


**Fig. 7.** Sample 5 and 6 from breccia corridor (see location Fig. 2) – (a) general aspect of a breccia sample 6 collected on the margin of the corridor; (b) Detail of geodic cavity with euhedral quartz partially filled with barite (sample 5); (c) same sample 5 in polished section showing the relationship between microtextures and mineral fillings; (d) relationship between euhedral quartz and granite matrix in sample 5 (polarized light); (e) cataclasite breccia clast crosscut by quartz veinlet in sample 5 (polarized light); (f) (g) Polished section of the cohesive cataclasite that deformed the older breccia in sample 6; (h) Alteration of biotite to clays (transmitted light) (sample 6); (i) Alteration of plagioclase to clay and microquartz (polarized light) (sample 6).

The granite clasts of the breccia and the granite matrix of breccia walls are intensely altered. A mixing of clay minerals (illite-smectite mixed layers) and iron-hydroxides replace rare biotite flakes (<5%) and a part of primary muscovite (Fig. 7-h), while K-feldspar and plagioclase grains are intensely dissolved and replaced by clay minerals (illite, illite-smectite mixed layers) and microquartz (Fig. 7-i). APS minerals are associated with illite in porosity of plagioclase dissolution. The average chemical formula of APS in granite (sample 1 and sample 5), as measured by electron microprobe, is:

$(Pb_{0.22}Ce_{0.30}Sr_{0.24}La_{0.14}Ca_{0.13})\ (Al_{0.9}\ Fe_{0.1})$
$(PO_4)_{1.30}(SO_4)_{0.14}(AsO_4)_{0.27}(SiO_4)_{0.22}\ (OH)_6$

Centimeters distant from the breccia, some biotite flakes (<5%) are altered to clay minerals (illite) with titanium oxides and iron hydroxides, while others exhibit greenish rims with hematite.

*4.2.3.2. Mineral sequence.* According to the macroscopic and microscopic observations, cement of cohesive cataclasites is silica/microquartz. The reddish color is mainly due to the abundance of iron hydroxides, whereas the greenish color is attributed to variable amounts of illite particles. Hematite, euhedral quartz then barite are more rarely present as mineral fills of opening-mode fractures intersecting cataclasite in their length or of residual macroporosity in breccia. Common alteration observed in the granite walls is marked by partial dissolution of K-feldspar and plagioclase, impregnation of plagioclase porosity by iron hydroxides, kaolinite then illite ± APS ± quartz, quartz filling in porosity of K-feldspar porosity and replacement of biotite by illite + chlorite + hematite and/or illite-smectite mixed layers + iron hydroxides.

All the mineral fillings in fractures and associated alterations are not contemporaneous, but precipitated from fluids present at different times in the porosity of the fracture network and the connected matrix porosity. The textural relationships between phases are informative of the relative chronology of the mineral fills and alterations (Table 2).

The iron hydroxides fill in porosity of plagioclase dissolution in granite matrix indicates that plagioclase dissolution is earlier than iron hydroxides formation. In the same way, a large part of iron hydroxides in fractures and matrix porosity are overlapped and cemented by microquartz ± illite, indicating that precipitation of iron hydroxides is earlier than formation of microquartz ± illite.

The opening-mode fractures affect the cohesive cataclasite, and are consequently later. The overlapping relations between hematite, euhedral quartz and barite filling fractures indicate that hematite and quartz precipitated first, possibly as the fracture opened. The fracture was subsequently filled with barite. Euhedral quartz in residual porosity of breccia precipitated probably contemporaneously of quartz in opening-mode fractures and in porosity of K-feldspar dissolution. Iron hydroxides associated with clays (illite-smectite mixed layers, kaolinite) are assumed to be associated with present-day weathering. The table summarizes the succession of mineral fills with time (Table 2).

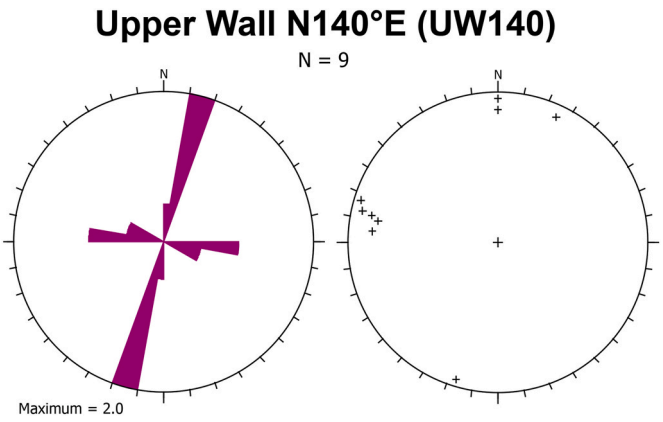


**Fig. 8.** Rose diagram of direction (10° classes, radius corresponds to 100% of maximum class) and projection of fracture poles measured in the Stephanian arkose. Schmidt diagram; equal area projection; lower hemisphere. N: Number of fracture data.

### 4.3. Fracture networks in arkose and diagenesis

#### 4.3.1. Fractures in arkose

The arkose contains fractures, but the layer is not easily accessible, limiting the observations and measurements (Fig. 2-B). Fractures are not mineral filled but show protocataclase. As the layer is eroded, the length of fractures is not possible to estimate. Most of them stop at the lower sediment limit (with the granite), but some continue in the granite. These constitute the E-W fault (Fig. 2-B).

As the accessibility is difficult, only nine fracture orientations were measured. While a statistically minimal sample, inspection of the outcrop suggests these measurements are representative and provide some limited information about orientation modes for the fractures in the arkosic rocks. The primary set strikes N10°E±10° and the secondary set strikes N100°E±10° (Fig. 8). All fractures have steep dips, nearly vertical and normal to bed dip.

#### 4.3.2. Arkose diagenetic sequence

Kushnir et al. (2018) performed petrophysical measurements, including porosity, P-wave velocity, permeability, uniaxial compressive strength, and thermal properties, on twelve samples collected in the Saint Pierre Bois quarry. We used these samples, named SPB1 to SPB12, to complete the mineralogical observations of the arkose matrix.

All these arkose rocks have almost similar petrographic features. They are heterogranular medium to coarse-grained arkoses (Fig. 9). Detrital minerals consist of quartz ($Qz_d$), plagioclase, and K-feldspar ($Kfs_d$) grains, with minor phyllosilicates (<5%), including biotite, muscovite and clays, tourmaline, iron hydroxides, and heavy minerals such as zircon, apatite, ilmenite, titanium oxides, and monazite. Authigenic minerals are primarily quartz with minor K-feldspar ($Kfs_1$),

**Table 2**
Relative chronology of the mineral fills in fractures crosscutting granite and the associated mineral precipitation and dissolution in the granite matrix at the walls of the fractures.

| | Mineral fills in fractures | Associated granite matrix | |
|---|---|---|---|
| | | Minerals fills in matrix porosity | alteration |
| Stage 1 | microquartz FeOx, clays | FeOx + clays in porosity of plagioclase dissolution | Feldspar dissolution<br>biotite, muscovite → FeOx + clays (illite/smectite, vermiculite) |
| Stage 2 | Microquartz illite euhedral quartz barite | Illite + quartz + APS in porosity of plagioclase dissolution<br>Quartz in porosity of K-feldspar dissolution | Partial dissolution of feldspars Partial alteration of K-feldspar and plagioclase to illite-mica<br>Biotite → Illite + chlorite + hematite |
| Stage 3 | FeOx, Clays Microquartz ? | FeOx, clays in porosity of feldspar dissolution | Feldspar dissolution<br>Plagioclase → kaolinite |

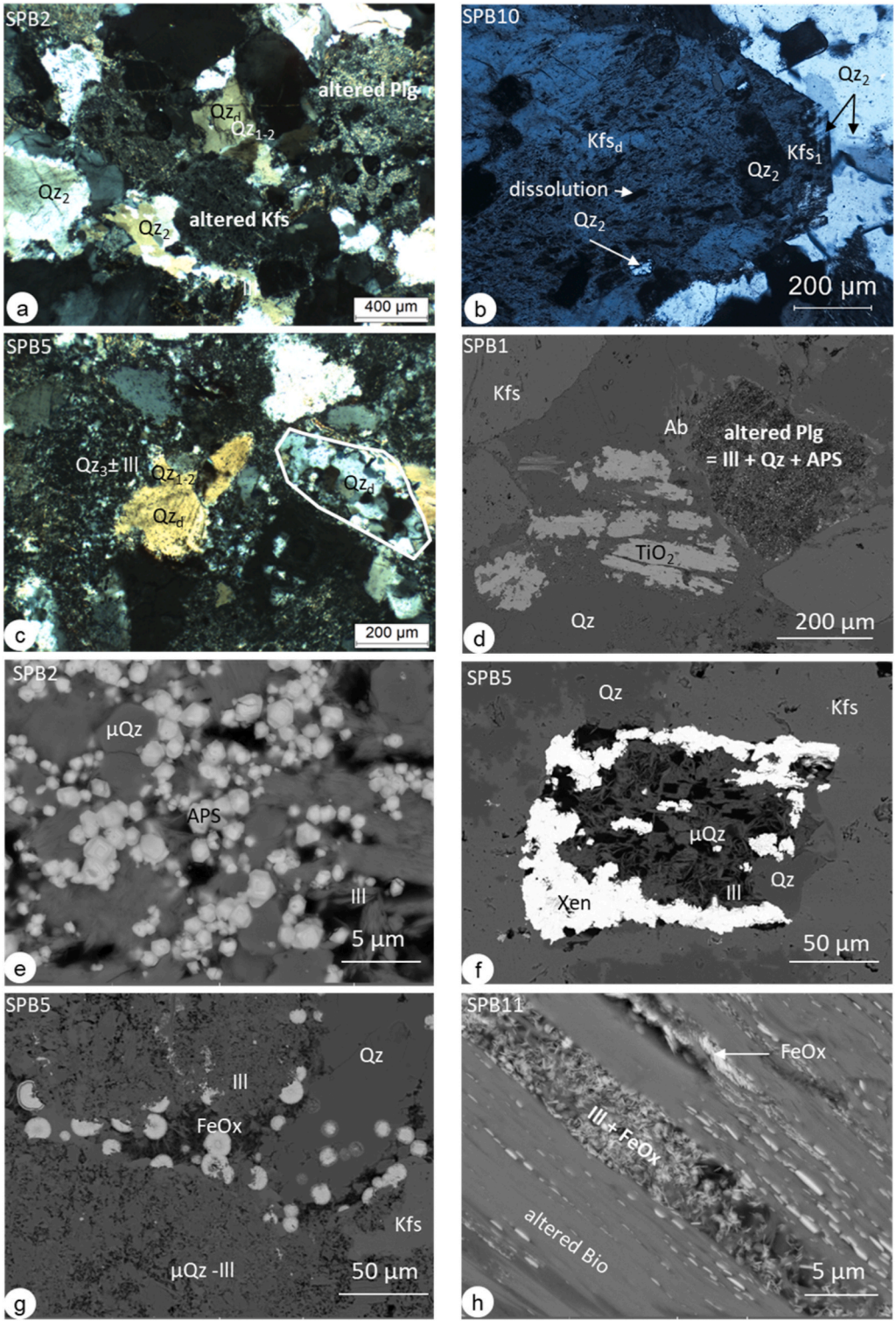


**Fig. 9.** Deformation and diagenesis in arkoses – (a) micrograph in polarized light showing the general texture of arkose (SPB2); (b) micrograph in polarized light showing authigenic K-feldspar ($Kfs_1$) growing on a detrital K-feldspar grain ($Kfs_d$). The both are affected by dissolution processes. Authigenic quartz ($Qz_2$) partially fills porosity of K-Feldspar dissolution (SPB10); (c) micrograph in polarized light providing evidence of protocataclasis in arkose (SPB5) identified by microquartz ($Qz_3$) and illite (Ill), alteration of feldspars and recrystallization of detrital quartz; (d) BSE image showing $TiO_2$, K-feldspar partially dissolved and altered plagioclase (Plg) partially replaced by illite and APS. A rim of albite (Ab) surrounds plagioclase grain (SPB1); (e) BSE image of APS and diagenetic illite in plagioclase dissolution porosity (SPB2); (f) phantom of mineral replaced by xenotime (Xen), microquartz (µQz) and illite (SPB5), (g) residual porosity filled by low-temperature radial iron hydroxides (SPB5); (h) biotite altered to clay and iron hydroxides (SPB11).

clay minerals including illite (Ill), APS minerals, galena and pyrite (Fig. 9). Pressure-solution features and a high degree of quartz recrystallization associated with deformation in presence of fluid commonly obliterate the pristine morphology of detrital quartz grains (Fig. 9a). However, rare preserved detrital quartz grains are generally sub-rounded to rounded based on the dust-lines that separate the detrital grain and quartz overgrowths.

At least two types of authigenic quartz are identified in all arkose samples (SPB2, Fig. 9a and b), based on their texture and relationships with other minerals:

1) early quartz aureoles ($Qz_1$) growing in continuity with detrital quartz crystals, where most of these quartz aureoles have irregular edges suggesting dissolution/recrystallization; and
2) xenomorphic quartz fillings in intergranular spaces and a portion of secondary porosity related to feldspar dissolution ($Qz_2$), where this

quartz is the major type observed in arkose. Another generation of micron-to medium-grained quartz crystallized at arkose grain contacts ($Qz_3$), corresponding to a protocataclastic texture. This latter was observed in samples SPB5 and SPB10 in the eastern part of the quarry (Fig. 9c).

About 10% of detrital grains are albite-dominant plagioclase. Pure albite surrounds detrital grains. Most plagioclase grains are sericitized (oriented clay particles) or exhibit a high degree of dissolution (Fig. 9a). An unoriented Mg-rich clay mineral phase associated with micron-sized euhedral grains of APS and microquartz has partly filled dissolution porosity (Fig. 9d and e). X-ray diffraction and electron microprobe analysis of clay separates provide evidence of pure illite (supplementary data). The average chemical formula of APS measured by electron microprobe is:

$(Pb_{0.38}Ce_{0.30}Sr_{0.29}La_{0.16}Ca_{0.09})$
$(Al_{0.9}\ Fe_{0.1})\ (PO_4)_{1.30}(SO_4)_{0.15}(AsO4)_{0.44}(SiO_4)_{0.11}\ (OH)_6$

K-feldspar comprises about 15–20% of detrital grains and their Ba content as measured by electron microprobe reaches up to ~0.14 wt %, whereas the Ba content in authigenic K-feldspar is below the detection limit. Detrital K-feldspar grains have various morphologies from rounded to almost euhedral grains, suggesting that the source of detrital K-feldspar was not far from the sedimentation site. K-feldspar is more abundant than plagioclase. Its degree of alteration/dissolution is also less than that of plagioclase, and even small euhedral authigenic K-feldspar is present on detrital grains (Fig. 9b). On the other hand, both authigenic and detrital K-feldspar grains provide evidence of dissolution, indicating that the dissolution process occurred later than authigenic K-feldspar cementation (Fig. 9b).

Detrital ferromagnesian minerals are brownish to greenish biotite, muscovite, tourmaline, and probable cordierite. Muscovite and tourmaline are mostly preserved, whereas biotite was commonly transformed into chlorite or illite and iron hydroxides (Fig. 9h). Rare cordierite is transformed into fine-grained mixture of muscovite and chlorite.

Among accessory minerals, zircon, monazite and titanium oxides (Fig. 9d) are mostly preserved, whereas ilmenite exhibits a high degree of dissolution and is partially replaced by secondary titanium oxides. Several detrital titanium oxide grains in the arkose provide evidence of chemical zoning in backscattered electron image and tungsten was detected by EDS. Trace element analyses using an electron microprobe made it possible to detect the presence of Fe, Sc, Nb, Ta, Cr, W and Sn in various amounts. Secondary xenotime partially fills plagioclase porosity, along with illite and microquartz (Fig. 9f).

In a similar way as in granite, textural relationships between minerals described above enabled the relative chronology of mineral dissolution, alteration and precipitation (Table 3).

**Table 3**
Relative chronology of diagenetic minerals in arkoses.

| | Minerals fills in matrix porosity | Alteration and dissolution |
|---|---|---|
| Early diagenesis | K-feldspar on detrital K-feldspar quartz aureole on detrital quartz | |
| Cataclasis ? | Microquartz | |
| Stage 2 | Illite + quartz + APS in porosity of plagioclase dissolution<br>Quartz in porosity of K-feldspar dissolution<br>Quartz, Barite, galena, pyrite in residual porosity | Feldspar dissolution<br>Biotite → Illite + chlorite + hematite |
| Cataclasis ? | Microquartz | |
| Stage 3 | FeOx, clays in porosity of feldspar dissolution | Feldspar dissolution<br>Plagioclase →kaolinite |

### 4.4. Porosity measurements

#### 4.4.1. Granite

Using the triple-weighing method, we measured bulk porosity of eight granite samples, including the six specimens collected along the E-W trending fault and fracture surfaces (samples 1 to 6 described in the § 4.2.3), one in the brecciated granite (sample 7) and one in the unaltered granite (sample 9, Fig. 2-A) This rock has a low porosity of 2.62% (Table 4). By comparison, porosity values of breccias and cataclasites sampled in the six fracture and fault surfaces (sample 1 to 6) and brecciated granite (sample 7) are more heterogeneous in terms of porosity, ranging from 1.65 to 7.45% (Table 4).

Porosities of cohesive cataclasites cemented by quartz (samples 1, 2 and 4) range between 1.65 and 2.62% (Table 4). The cataclasite cemented by iron hydroxides (sample 3) has a higher porosity of 5.73% (Table 4). Porosity in brecciated granite that shows protocataclastic texture (sample 7) is of 2.62% (Table 4). Porosities that are measured in breccia along the long fault surface (>30 m) crosscutting the sediment/granite transition (samples 5 and 6) are 4.5 and 7.45% (Table 4). These values represent an average porosity of the reworked granite matrix (including breccia), barite filling, and cohesive cataclasite. The granite on the margins of the breccia in sample 5 has a matrix porosity of 5.73% (Table 4).

Cohesive cataclasite crosscutting the breccia in sample 6 was not large enough to measure porosity using the triple-weighing method, but large enough to measure He and Hg porosities successively. A slab of the cataclasite provided evidence of two zones, an external reddish area and an internal orange region (Fig. 7 f,g), which were analyzed separately. The reddish cataclasite zone, which is well cemented by iron hydroxides, has He porosity of 6.74%, whereas the orange zone, which is well cohesive cataclasite cemented by silica/microquartz has He porosity of 2.13% (Table 4).

**Table 4**
Porosity measurements in breccia and cataclasis corridors affecting granite and granite wall rocks and in arkose.

| Samples | Weight (g) | Porosity type | Porosity (%) | Real volumic mass (g/cm) | Apparent volumic mass (g/cm$^3$) |
|---|---|---|---|---|---|
| **Sample 1** | | | | | |
| Matrix | | BSE | 3.7 ± 1.4 | | |
| Cataclasis - µQtz + Brt | | BSE | 4.5 ± 0.1 | | |
| Cataclasis - µQtz + Brt | | water | 2.62 | 2.64 | 2.57 |
| **Sample 2** | | | | | |
| Cataclasis - Qtz + Brt + Hem vein | | water | 1.65 | 2.75 | 2.71 |
| **Sample 3** | | | | | |
| FeOx | | water | 5.73 | 2.64 | 2.49 |
| **Sample 4** | | | | | |
| Breccia | | water | 2.05 | 2.63 | 2.58 |
| **Sample 5** | | | | | |
| Bulk breccia | 670.87 | water | 4.50 | 2.65 | 2.53 |
| Bulk breccia | | BSE | 3.4 ± 1.2 | | |
| Bulk granite | | water | 5.73 | 2.64 | 2.49 |
| **Sample 6** | | | | | |
| Bulk breccia | 3388.59 | water | 7.45 | 2.66 | 2.46 |
| Cataclasite | | Hg | 1.41 | 2.5883 | 2.5517 |
| orange part | | He | 2.13 | 2.6074 | 2.5517 |
| Cataclasite | | Hg | 5.42 | 2.5966 | 2.4558 |
| reddish part | | He | 6.74 | 2.6333 | 2.4558 |
| **Sample 7** | | | | | |
| Bulk granite breccia corridor | | water | 2.62 | 2.64 | 2.57 |
| **Sample 9** | | | | | |
| Bulk granite | | water | 2.62 | 2.64 | 2.57 |
| Bulk arkose | | water | 13.8 | 2.64 | 2.28 |

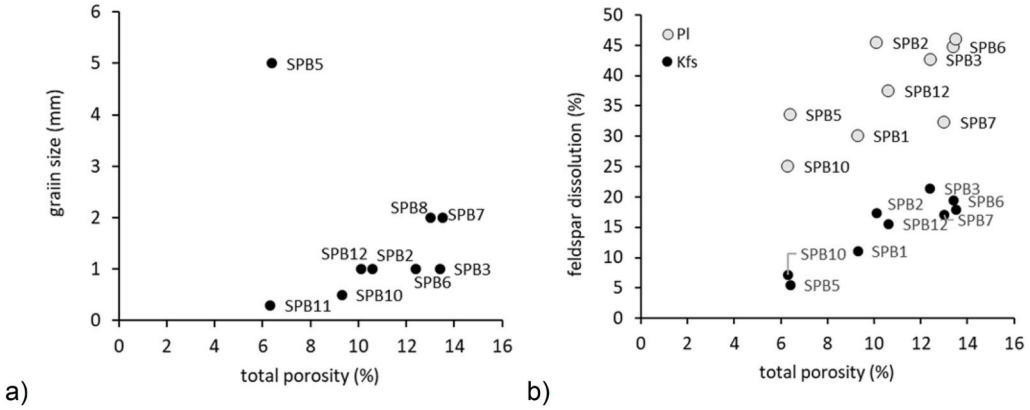


**Fig. 10.** a) relationship between total porosity and maximum grain size as related to feldspars in the arkose; b) relationship between total porosity and secondary porosity due to dissolution of both feldspars: K-feldspar (Kfs) and plagioclase (Pl).

**Table 5**
U, Th concentrations and various measured isotopic ratios. Ratios given in (in parenthese) in headings are activity ratios. Analytical uncertainties (in parentheses) are given as 2σ.

| Sample | U (μg/g) | Th (μg/g) | ($^{234}$U/$^{238}$U) | ($^{238}$U/$^{232}$Th) | ($^{230}$Th/$^{232}$Th) | ($^{230}$Th/$^{238}$U) | ($^{230}$Th/$^{234}$U) |
|---|---|---|---|---|---|---|---|
| SPB 3.2 | 10.22 (12) | 18.25 (02) | 1.1426 (33) | 1.699 (20) | 2.298 (19) | 1.353 (16) | 1.184 (14) |
| SPB 3.3 | 7.80 (10) | 18.39 (01) | 1.1920 (33) | 1.286 (17) | 1.824 (15) | 1.418 (18) | 1.189 (15) |

**Table 6**
Geochemical parameters used for the model. Values in italics refer to the initial assumptions (see above) and/or to possible realistic values (U and Th contents, U and Th activity ratios for the incoming water component). Values in plain characters are derived from calculations.

| Sample | Uinit. (μg/g) | Thinit. (μg/g) | ($^{234}$U/$^{238}$U) | ($^{230}$Th/$^{232}$Th) | ($^{230}$Th/$^{234}$U) |
|---|---|---|---|---|---|
| SPB 3.2 | *15.0* | *18* | *1* | 2.61 | *1* |
| SPB 3.3 | *11.5* | *18* | *1* | 2.00 | *1* |
| Incoming water | *1E-03* | *1E-06* | *2* | *3.70* | 6.05E-04 |

Mercury porosity measurements provide information on bulk porosity and pore size distribution (SD-porosity). The difference between the He and the Hg porosities, which corresponds to porosity attributed to pore sizes <3.67 nm, is estimated at 1.32% in the reddish part and 0.72% in the internal part. Pore sizes in both zones show a bimodal distribution with the same pore size population: a first group with sizes ranging from 0.004 to 1 μm with a maximum at 0.02 μm, and a second group of 100 μm-sized pores. Comparison of data from both parts of the cataclasite shows that macropores do not seem to be filled by microquartz cement.

### 4.4.2. *Arkose*

Total porosity and dissolution porosity of both types of feldspars

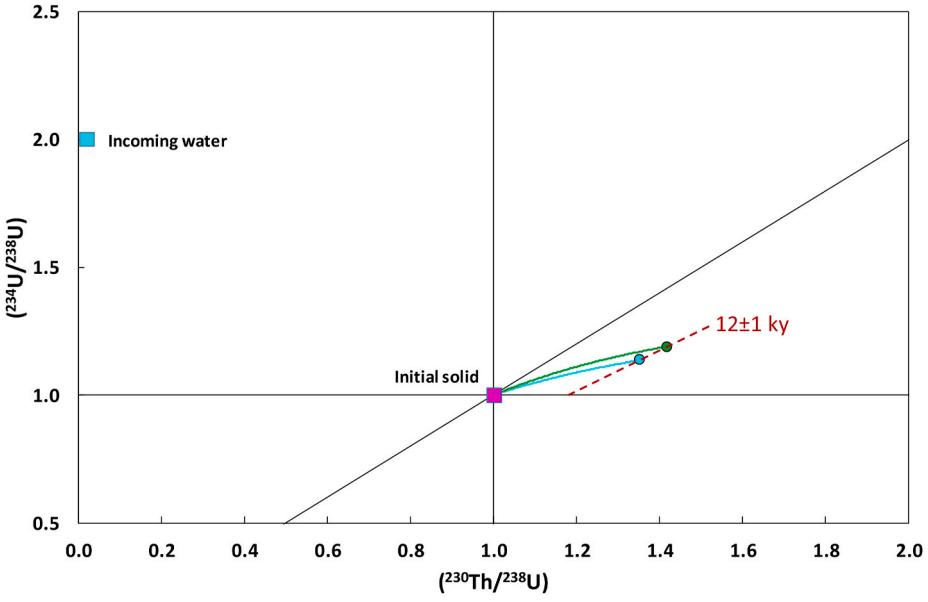


**Fig. 11.** $^{234}$U/$^{238}$U versus $^{230}$Th/$^{238}$U diagram showing a possible evolution model for the two iron hydroxides filling major fracture 16SPB3. SPB 3.2 is plotted in blue and SPB 3.3 in green. See text for more detailed explanation. (For interpretation of the references to color in this figure legend, the reader is referred to the Web version of this article.)

were measured by treatment of backscattered electron images (SD-porosity data) in the twelve samples of arkoses (SPB1 to SPB12) collected in the eastern part of the quarry by Kushnir et al. (2018). The total porosity of arkose in sample 9 was measured by water porosity. Total porosities measured by water porosity and by image treatment (Φ) range between ~5 and 14% (Table 4), and are consistent with He porosities of Kushnir et al. (2018). They are representative of the connected porosity in arkose. Total porosity of samples SPB1 to SPB12 is relatively well correlated with grain size. Feldspar dissolution porosity provides evidence of a positive correlation between total porosity and porosity of plagioclase and K feldspar dissolution (Fig. 10a; Fig. 10b). In all cases, plagioclase dissolution porosity is significantly greater than K feldspar dissolution porosity. The smallest porosity values are associated with two samples SPB5 and SPB10 that have protocataclastic or fine-grained texture and K-feldspar porosity filled by quartz.

### 4.5. Geochemistry

#### 4.5.1. Trace elements in different generations of quartz from the granite

We identified various generations of quartz in the granite matrix and fractures based on their textural relationships, morphology, and size. However, it remains challenging to distinguish all generations under the microscope, due to polyphase tectonics and fluid circulation. For this reason, we analyzed 22 trace elements in different quartz generations, among them magmatic quartz and pegmatitic quartz in a granite sample 8, and euhedral quartz partially filling macroporosity in breccia collected on the long (>30 m) fault surface (sample 5). Among the 22 trace elements that were analyzed, only Li, Al, Ti, Sc, Ge, As, and Sb are detected (SD-trace elements).

Magmatic quartz has high Sc (4.6–5.8 ppm) and Ti (4.8–8.1 ppm) concentrations and the lowest Li (21–53 ppm), Al (151–265 ppm), and Ge (0.8–1.3 ppm) values. In pegmatitic quartz, Sc concentrations remain high (3.8–6 ppm), whereas Ti values are very low (0.7–1 ppm) and Li (34–47 ppm), Al (236–335 ppm), and Ge (2.1–2.5 ppm) values are higher. Magmatic and pegmatitic quartz do not contain other metals (if present, they are below detection limits). Comparatively euhedral quartz in macroporosity of breccia has very low Ti (0.1–0.3 ppm) and Sc (2.4–3.4 ppm) concentrations, the highest Li (623–1043 ppm), Al (2140–2673 ppm), and Ge (7–13.3 ppm) values, and significant traces of As (3.3.-21.7 ppm) and Sb (3.6–5.4 ppm).

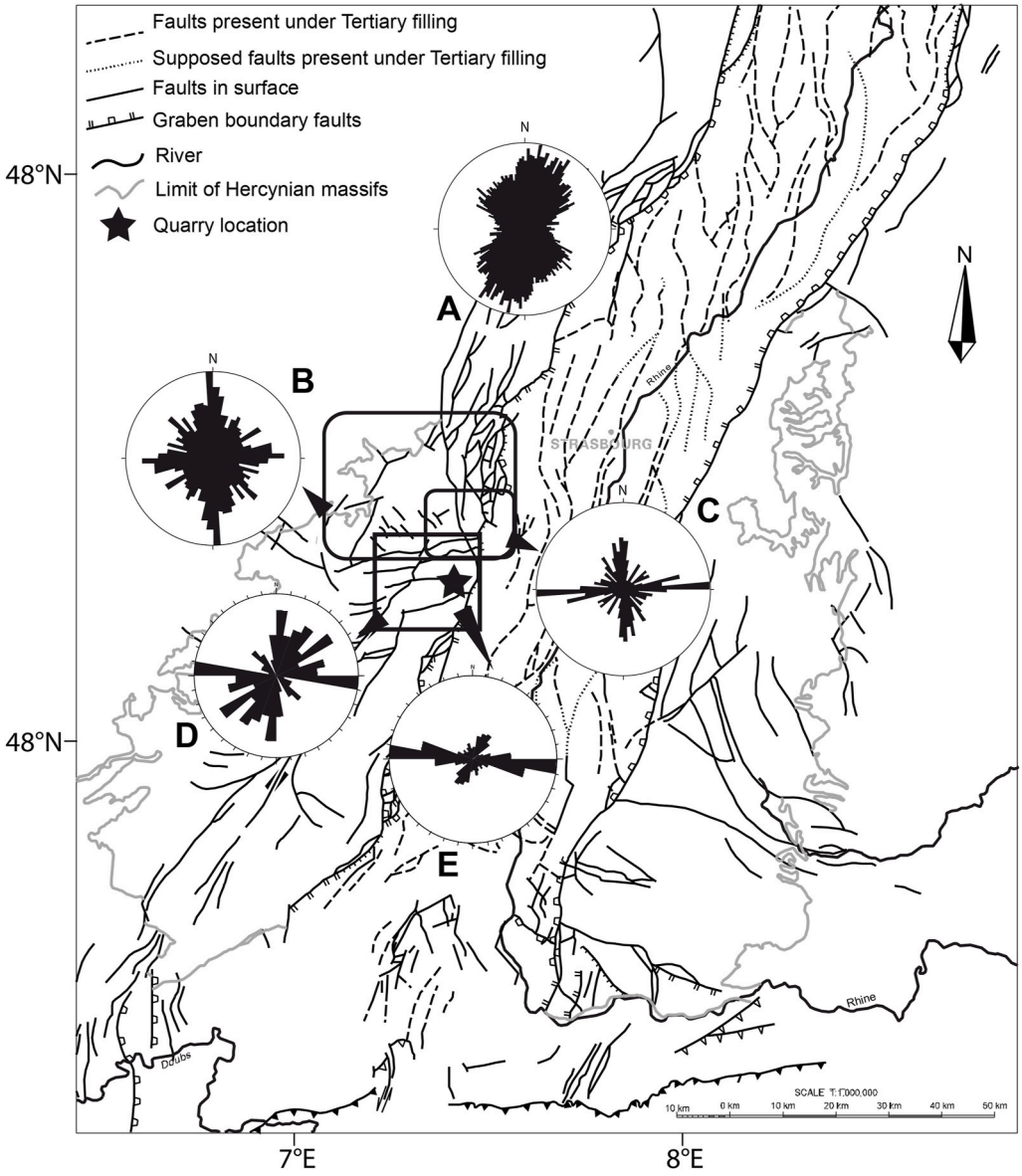


**Fig. 12.** Main directions of fracture sets analyzed based on (A) fault trace map of the Rhine graben and its margin from Valley (2007), (B) and (C) lineaments on DTM (Digital Terrain Model) from Bertrand et al. (2018), (D) geologic map at 1/50 000[e] (Blanalt et al., 1972), (E) this study, all fractures (number of data: 238).

#### 4.5.2. U–Th systematics on iron hydroxides

For U–Th measurements, we selected iron hydroxides that fill a major fracture in the altered-fractured zone on the eastern side of the quarry (sample 3). Two aliquots of sample were prepared and analyzed. Results are reported in Table 5.

Both samples display relatively high U concentrations, with a slightly higher U content for sample 3.2 compared to sample 3.3. In contrast, Th concentrations are similar in both aliquots (Table 5). Present-day Th/U ratios are 1.8 and 2.4 for sample 3.2 and sample 3.3, respectively. Such values are clearly lower than those of the upper continental crust (~4), (Taylor and McLennan, 1995; Wedepohl, 1995).

Uranium activity ratios are similar in the both aliquots and are slightly but significantly higher than the value of secular equilibrium (Table 5). This implies that the system is open at present for uranium, or at least has been open for the last million years. $^{230}Th/^{234}U$ and $^{230}Th/^{238}U$ activity ratios in the two aliquots are also higher than 1, indicating uranium loss because Th is usually considered to be generally insoluble during water/rock interaction processes.

Simple uranium loss is inconsistent with the data. Water/mineral interaction processes are likely to result in a $^{234}U/^{238}U$ ratio lower than 1 in the solid phase, and inversely, higher than 1 in the interacting water, due to the preferential leaching of $^{234}U$ in the solid phase as a result of α-recoil processes (Fleischer, 1980).

Thus the most probable hypothesis to explain the data calls for open-system evolution with a U input from interacting water (thus probably having a $^{234}U/^{238}U$ activity ratio higher than 1) and a concomitant loss of U in the solid. The following possible evolution model has been tentatively derived, based on the following assumptions regarding the geochemical characteristics of incoming water and the initial solid:

- a single-stage model open-system evolution,
- gain and loss of U do not vary through time,
- both follow an exponential law (order 1),
- the $^{238}U$ decay chain is initially at secular equilibrium in the solid,
- Th remains immobile during the open-system evolution.

Differential equations of a U-series open-system evolution model through time have been described and can be found in a number of references (Chabaux et al., 2003). Modelling parameters are given in Table 6.

Data have been plotted in a $^{234}U/^{238}U$ versus $^{230}Th/^{238}U$ diagram (Fig. 11). A reference age of 12 ± 1 ky for the two samples can be derived, featuring similar loss and gain of U:1.7 ± 1 $10^{-5}$ $year^{-1}$ and 4.56 ± 0.06 $10^{-5}$ $year^{-1}$, respectively.

## 5. Discussion

### 5.1. Origine of the fracture network

The three zones with various alteration, the highly altered zone in the south-east part of the quarry, the slightly altered and fractured zone in the western and northern parts and the mixed zone between both, are part of a larger fault zone, and are defined as the core zone, damage zone and transition zone, respectively. The core zone, more than 50m thick, is composed of comminuted rock, breccia, protocataclasite, cataclasite, which suppose a high degree of fracture connectivity, and with more rarely ductile deformation bands in the granitic basement (Fig. 2-E and F). The larger faults in this comminuted rocks are mainly E-W (set 1) and cross the arkose/granite transition. These main faults show cataclastic border in the granite and protocataclasites in the arkose.

The transition between the fault core and the damage zone corresponds to a collapse area limited with the damage zone by a polyphase breccia corridor (Fig. 2-C) and with the fault core by the wide bleached E-W fault surface that cross almost half of the eastern side of the quarry (Fig. 2-E). In this transition zone, around 20–25m thick, some E-W faults cross and displace the granite/arkose transition of about 1 m with a normal movement. Thereby, the total offset in this zone is about 10m.

In the western and northern parts of the quarry, the damage zone, more than 100m thickness, constituted by non-comminuted rocks but is largely fractured including the two dominant fracture directions (Fig. 3), is uplifted of around 10m compared with the core zone.

The study area is located in a highly fractured region affected by a long tectonic history (Edel et al., 2007; Rotstein et al., 2006; Schumacher, 2002; Villemin and Bergerat, 1987). As a result, all scales of fractures are present. At the large regional scale, Valley (2007) analyzed the fault trace map and highlighted the primary direction of major structures that make up the graben and its vicinity. Three major directions predominate. A N0°E-N20°E direction (Fig. 12-A), known as the Rhenish direction, corresponds to the normal boundary fault that formed the Upper Rhine Graben during the Oligocene (Schumacher, 2002; Villemin and Bergerat, 1987) and possibly reactivated a Hercynian structure called the Upper Rhenish Shear Zone (Edel et al., 2007; Illies, 1972; Rotstein et al., 2006). A second main direction is NE-SW and the third is NW-SE (Fig. 12-A), both linked to Hercynian tectonics (Schumacher, 2002). The NE-SW direction being the direction of major Hercynian dislocation zones, such as the Lalaye-Lubine fault zone. At this scale, the E-W direction is poorly represented (Fig. 12-A).

At a smaller scale, in the northern part of the Vosges Massif, Bertrand et al. (2018) analyzed the lineament using a DTM (Digital Terrain Model) with various lighting and showed several main sets (Fig. 12-B and C). The three main directions cited above are present: N–S representing 25% of the total; NE-SW, 10%; NW-SE, 15%, and two others, ENE-WSW and E-W directions representing 5% and 10%, respectively (Bertrand et al., 2018, Fig. 12-B). These authors focused on the south-eastern part of the zone, just north of the Lalaye-Lubine fault zone and the Saint Pierre Bois quarry, and showed that in this area, the E-W direction predominates, accounting for 23% of the lineaments (Bertrand et al., 2018, Fig. 12-C).

South of the Lalaye-Lubine fault zone, we digitalized the fault traces on the local 1/50 000$^{e}$ geological map (Blanalt et al., 1972). The analysis shows four main directions: E-W, N–S, NE-SW, and to a lesser extent NW-SE (Fig. 12-D). The E-W direction constitutes the main set as in the northern area analyzed by Bertrand et al. (2018) (Fig. 12-B).

Whereas the main directions are equivalent, the distributions of each set are different in the Vosges Massif and in the Rhine Graben. The Hercynian directions, mainly NE-SW and NW-SE, are more common than the Rhenish direction (N–S) in the Vosges Massif (Fig. 12). However, the E-W direction, which is mainly present in the Saint Pierre Bois quarry (Fig. 12-C and D) and its surroundings, is less frequent at the Rhine graben scale (Fig. 12-A and B). This fracture set could be related to Hercynian tectonics and linked to the direction of the Villé basin, which opened during the Permian at the end of the Hercynian orogen.

Considering the tectonic history of the area, the large E-W fault zone crossing the quarry could be in relation with the Saalian tectonic phase which has an ESE-WNW to NW-SE-oriented stress field (Bergerat, 1987). This constitutes the last Hercynian compression phase during the Saxonian before the formation of Permo-Triassic basins, such as the Villé basin. This E-W fault zone direction also matches to the Lalaye-Lubine fault zone, which corresponds to the Hercynian suture between the Saxo-Thuringian and the Moldanubian domains (Fig. 1-B).

In the damage zone, the fracture pattern can be compared to those defined by Bertrand et al. (2018) in the northern part of the Vosges massif. In this area, these authors define three orders of blocks separated by three orders of fractures. In our study, located further south and at another scale, the fracture pattern, represented by F1 and F2, are slightly different to the central block of Bertrand et al. (2018). As these authors observed further north, it appears a difference of final state of fracture network between the central block and the southern block, where it is located the Saint Pierre Bois quarry. As the fault zone, the F1 fracture set appears clearly linked to the Hercynian faults in the granite, which show also a dominant E-W magmatic fabric direction (Skrzypek, 2011), as the F2 fracture set (Arthaud and Matte, 1975). These fractures constituted a

structural heritance reactivated during the latter deformation (Illies, 1972; Schumacher, 2002) and pathways for fluid circulation at different times.

### 5.2. Mineralization, fluid/rock interactions and their timing

The faults crosscutting the arkose/granite transition rather favored fluid circulation through the granite and arkose. Fluid circulations are inferred from the mineralization in fractures, and mineral and chemical changes in the rock matrix due to water/rock interactions, and their timing. Petrology and chemistry of fracture filling minerals in the granite and diagenetic minerals cementing the overlying arkoses provide evidence of almost similar processes of alteration, dissolution and precipitation in porosity of the two lithological compartments.

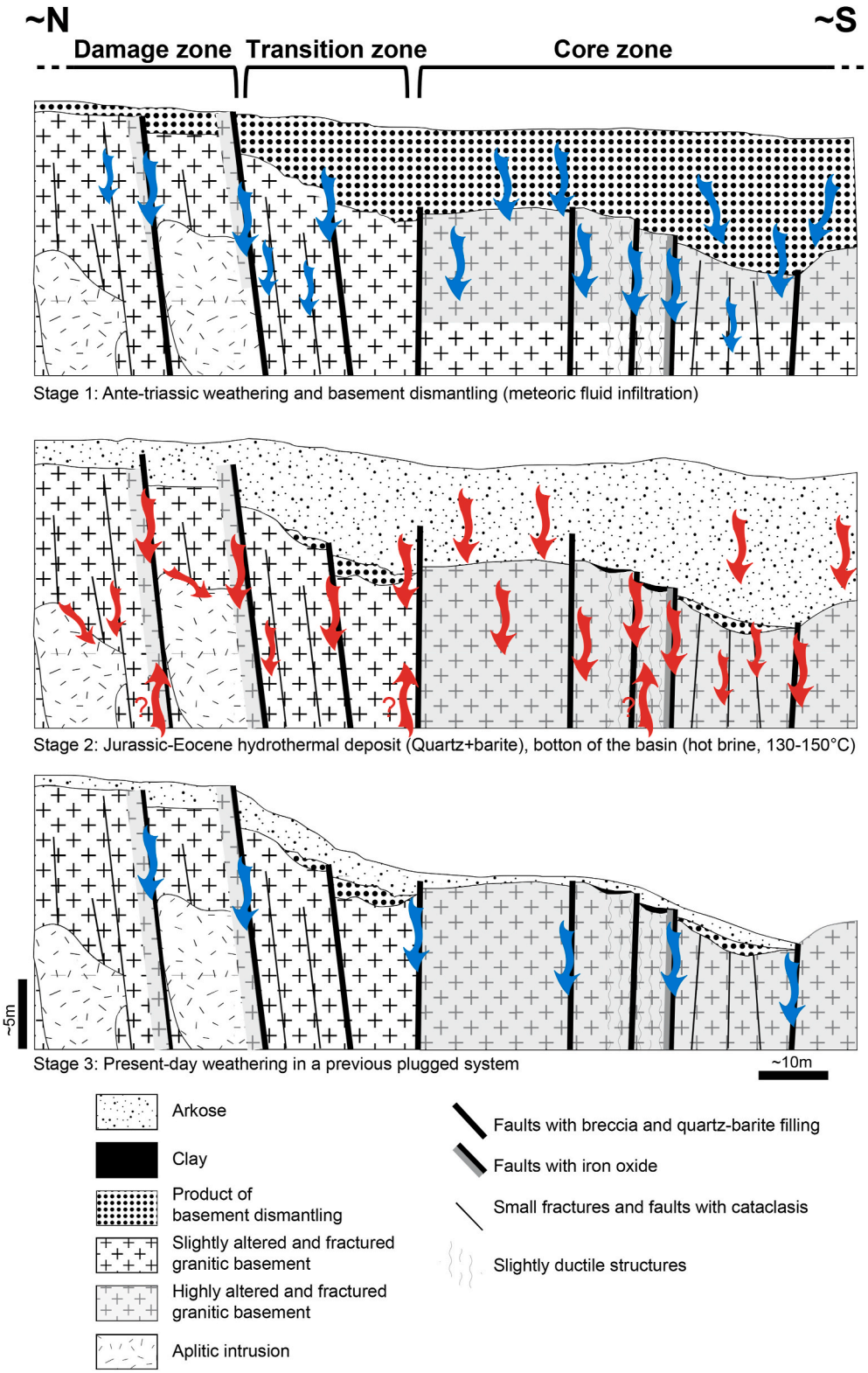


**Fig. 13.** Conceptual model of evolution of fluid circulation in the Saint Pierre Bois quarry.

The microquartz ± illite mineral assemblage is present in cataclasite, protocataclasite and breccia in granite fractures and matrix (Stage 2 - Table 2), and in protocataclasite and in quartz intergrains in arkose (Stage 2 - Table 3). Some coarser quartz, euhedral in granite and xenomorphic in arkose, and barite precipitated later in residual porosity of granite breccia and arkose. Fluid/granite and fluid/arkose interactions associated to this stage are the alteration of biotite into chlorite + illite + hematite, precipitation of illite 2M + APS + quartz in porosity of plagioclase dissolution, and precipitation of quartz in porosity of K-feldspar dissolution. Trace elements such as Pb and As, incorporated in euhedral quartz in granite and in APS in plagioclase porosity in both granite and arkose, strongly suggest that illite 2M, APS, and quartz with minor sulfides (galena and pyrite) in the granite matrix and arkose porosity are associated with this stage. Most of the trace elements present in minerals of this stage (Al, Ge, Li, Sc and As in quartz, Al, As, Ce, La, S, Sr and Pb in APS, Sc, Nb, Ta, Cr and Sn in titanium oxides, Pb and S in galena), and consequently in the fluid from which they precipitated were initially present as traces in primary feldspars and biotite of granite (Drüppel et al., 2020), and resulted from their destabilization. It is noteworthy that the Ti concentrations of 5–8 ppm measured in some quite well-preserved magmatic quartz of the Dambach granite are significantly lower than literature values (Allan and Yardley, 2007), probably due to recrystallization and fluid/quartz interactions (Haertel et al., 2013; Wark and Watson, 2006). This point is important, because it suggests that the least altered granite is affected by fluid-assisted deformation, remobilizing trace elements such as Al and Ti in the rock.

Illite formation indicates temperatures of at least ~130–150 °C (Liewig and Clauer, 2000). Hydrothermal alteration in granite matrix are consistent with chemical alterations observed during experiments of fluid/rock interactions between granite of the Schwarzwald (eastern shoulder of the graben) and NaCl-rich fluids at 200 °C (Drüppel et al., 2020). Such temperatures are higher than those attained at maximum burial of the sediment cover/basement in the eastern part of the Paris Basin transition prior to graben formation (Blaise et al., 2014). They were induced by an abnormal thermal gradient associated with volcanism during the graben formation in the Tertiary (Sittler, 1992). Early cataclastic textures and hydrothermal quartz, illite and barite formed at ~140–150 °C of Saint Pierre Bois are comparable to that described in faults crosscutting the Hercynian crystalline basement of the URG, such as the E-W Schauenburg fault zone on the east shoulder of the graben (Schleicher et al., 2006), or the fractures of the EPS1 well of the EGS Soultz site inside the graben, or NE-SW fractures in granite of the Waldhambach quarry on its west shoulder (Dezayes and Lerouge, 2019), which precipitated from deep hot hydrothermal fluids at the sedimentary cover/Hercynian granitic basement transition in the URG at Tertiary prior to its collapse (Dezayes and Lerouge, 2019; Genter et al., 2010; Walter et al., 2015).

The second common mineral assemblage consists of iron hydroxides with minor clays and microquartz that fill residual porosity in granite fractures, faults, and breccia corridors in granite and in the arkose matrix. This stage is associated to a low-temperature alteration (weathering) of the primary magmatic minerals in granite and detrital minerals in arkoses that have not been affected by hydrothermal alteration, such as dissolution of K-feldspars, transformation of plagioclase into kaolinite and destabilization of biotite into illite-smectite mixed layers and iron hydroxides (Stage 3, Table 2, Table 3). Earlier hydrothermal minerals, such as quartz, illite and barite, are also affected by weathering processes. However, they are more resistant to weathering than feldspars and biotite, or are more difficult to identify such as illite and illite-smectite mixed layers. The iron hydroxides precipitated from iron liberated by destabilization of ferro-magnesian minerals such as biotite or chlorite, or remobilized by surficial fluids. U–Th measurements on iron hydroxides in an E-W fracture in the core zone provide evidence of recent weathering processes (<1 Ma) affecting granites of the Vosgian massif (Ackerer et al., 2016; Schaffhauser, 2013).

Textural relationships gave evidence of some iron hydroxides present in porosity of plagioclase and in fractures that were cemented by hydrothermal quartz and illite, and consequently formed earlier than them (Stage 1, Table 2, Table 3). This observation in most of the fracture fills in granite at the quarry scale provides evidence of weathering processes deep in granite prior to contemporaneous deposition of Stephanian arkoses, in agreement with Wyns (1999), Wyns et al. (2004) and Dezayes and Lerouge (2019). Even though it remains delicate to distinguish the two generations of iron hydroxides, it is important to not neglect this ancient weathering stage that was probably very similar to the present-day weathering in terms of chemical processes (feldspar dissolution, mica alteration), creating possible granite weakness and secondary porosity and favoring fracture network evolution and circulation of hydrothermal fluids (Callahan et al., 2020a,b).

### 5.3. Distribution of the mineralization in the fault zone

Mineral fillings and dissolution/precipitations in the wall rocks attributed to the hydrothermal stage associated with deep hot fluid circulation and those attributed to the recent weathering at surface are present in the three parts of the fault zone: the core zone, the damage zone and the transition zone, and in the both lithological compartments: granite and arkose. Their distribution in the three parts of the fault zone is informative on pathways of the different generations of fluids in the fault crosscutting the arkose/granite transition with time (Caine et al., 1996; Callahan et al., 2019, 2020).

The core zone in granite is characterized by abundant fractures that are filled by hydrothermal minerals and/or low-temperature iron hydroxides. The surfaces of the smallest fractures are cohesive cataclasites of low porosity (<2.6%) that are rapidly clogged by microquartz with minor illite. Breccia associated with faults that are not entirely filled by microquartz and illite are clogged by late hydrothermal euhedral quartz and barite. Porosities measured in the both types of structure are lower than 2.6%, and are consequently close to porosity of initial granite. Breccia associated with fault surfaces, that were not clogged by hydrothermal minerals are filled with <1 My-aged iron hydroxides, and have porosity of ~5–6%, higher than the granite reference, indicating that they remain the rare active fluid pathways. Granite matrix wall rocks are highly hydrothermalized then weathered, show no relics of primary ferro-magnesian minerals, and exhibit a high degree of alteration and feldspar dissolution (plagioclase and K-feldspar). In fractures filled with hydrothermal-stage minerals, feldspar dissolution porosity is filled by quartz. Observations suggest that if the fracture network and the pre-Triassic weathering processes created porosity, hydrothermal quartz with minor clays clogged a large part of it, which explains why the granite matrix porosity is almost close to granite porosity (Kushnir et al., 2018).

Contrastingly, Stephanian arkoses in the fault core show wide range of porosity between 3 and 16% (this study; Kushnir et al., 2018). Fluid pathways seem to be more associated with matrix porosity due to feldspar dissolution and intergrain boundaries than with a fracture network. The lowest porosity values (down to 3%) are measured in the arkoses affected by protocataclasis in the core zone. They are low porosity due to hydrothermal microquartz shear bands and to quartz filling residual porosity, including porosity created by K-feldspar dissolution. Here, the deformation leads to pore space collapse, grain crushing, and porosity reduction, as has been observed in deformation bands (Antonellini and Aydin, 1994).

While granite is highly fractured and altered in the fault core, the damage zone is characterized by E-W faults crossing a stiff granite that is barely altered. Most of the fractures and faults do not show aperture and are clogged by hydrothermal microquartz with illite, inducing low porosity values close to reference granite (2–3%). Among the E-W faults, one large (>30 m) cross the arkose/granite transition and contains breccia where porosity attains 7.5% corresponding to a macroporosity represented by mm-to cm-sized open cavities partially filled by euhedral quartz, and more rarely barite.

The transition zone is a mixed zone limited by two major E-W stiff and almost clogged breccias. Clogging is essentially due to intense cataclasis and hydrothermal microquartz cementation.

### 5.4. Evolution of the fluid pathways in the fault zone with time

The relative width of the core zone and damage zone rather suggests that the fault zone crosscutting the Saint Pierre Bois quarry early acted as a distributed conduit, according to Caine et al. (1996). However, fluid flow and fluid-rock interactions have contributed to change hydraulic and mechanical properties along the geological times, leading to its almost clogging. The integrated structural, petrological, and geochemical study of the fault zone crosscutting the arkose/granite transition in the Saint Pierre Bois quarry allowed reconstructing the evolution of the fault network architecture in term of structure, fluid/rock interactions and porosity/permeability, on the basis of previous models of fault architectural evolution (Callahan et al., 2020a,b and references therein) (Fig. 13):

(1) *Inheritance* may influence the initiation of faults (Crider, 2015). At the end of the Hercynian orogeny, the Dambach granite of Lower Carboniferous age uplifted and underwent erosion and weathered process (Stage 1 - Fig. 13). Even though we have evidence of pre-Triassic weathering (Wyns, 1999; Wyns et al., 2004; this work), it is not possible to evaluate its role (quantification of clays and dissolution de feldspars) on the petrophysical properties of granite at this period. At this stage, the suture between the Saxo-Thuringian and the Moldanubian domains was considered as a weak crustal zone (Edel and Fluck, 1989).

(2) *Reactivation* of inherited structures and development of new fractures with increasing deformation (Moir et al., 2010). This weak crustal zone allowed creating the collapse of the Villé basin and the formation of a dominate E-W fracture network. In this context, the formation of the E-W fault zone of Saint Pierre Bois during Permian results from the development and the coalescence of slip surfaces, including cataclasite and fault breccia, and ductile deformation bands affecting the Hercynian crystalline basement.

(3) The *high-temperature (130–150°C) hydrothermal stage* results from the burial of the basin and the downward circulation of the hot brine and possibly the upward circulation in the deeper part of the basin (Stage 2 - Fig. 13). This results in quartz precipitation corresponding to the precipitation-strengthening model of Callahan et al. (2020a,b). Silicified breccia of cataclasites and breccias at the limit between the damage zone and the transition zone is the only evidence of dilation and failure (Callahan et al., 2020a, b).

(4) At the present-day stage, E-W breccia faults cemented by iron hydroxides in the core zone and edges of the rare E-W breccia corridors crosscutting the arkose/granite transition in the damage zone remain pathways for present-day meteoric fluids (Stage 3 – Fig. 13), and could be potentially considered as efficient drains at depth.

## 6. Conclusions

This decametric-scale field study and petrographic analysis, including structural geology, petrological, petrophysical and geochemical analyses, in a Vosgian quarry identifies a previously unrecognized fault zone and its episodic mineralization.

- This fault zone crosses the sediment/basement transition, and shows a classical fault structure for crystalline rocks: core and damage zones, plus a transition zone:
  - The core zone (>50m thick) is highly fractured and then have probably high connectivity. In the granite, hydrothermal minerals (quartz, barite) clog many fractures, whereas others currently filled by recent iron hydroxides likely constituted active (open) flow pathways. On the other hand, in the arkoses, fluids circulate only through interconnected porosity of the matrix.
  - The transition zone (20–25m thick) contains E-W faults cross and displace the cover/basement transition. The total displacement is around 10m.
  - The damage zone (>100m thick) comprises non-comminuted rock that is fractured by two main fracture sets: E-W (set 1) and NNE-SSW (set 2). These fractures are randomly distributed in much of the quarry but locally fractures are concentrated in clusters. Some intervals lack fractures, where aplite and pegmatite intrude the granite. Hydrothermal minerals (quartz, barite) usually clog cavities along E-W faults but their edge, constituted by breccia, have a higher porosity and may constitute fluid pathways in the damage zone.
- The main E-W fracture set present in the damage zone is kinematically consistent with local Hercynian tectonic movement and the Saxonian opening of the Permian Villé basin. This interpretation presumes that the inferred fault zone shares an E-W strike.
- Evidence from alteration suggests that the fault zone constituted a good fluid pathway until the fault formation and which evolves during the regional tectonic history and the burial of the Villé basin.
  - Before basin opening, meteoritic fluids flowed in the granite and altered the core zone and the individual faults within the damage zone (Stage 1).
  - With the burial of the basin, probably from Jurassic to Eocene, hydrothermal fluids, hot brine (130–150 °C), circulated and to altered the fault zone, the granite through fractures and the arkose through its matrix (Stage 2).
  - The present-day fracture system is almost clogged by hydrothermal quartz deposits but the meteoric cold fluids circulate yet (Stage 3).

This fault zone model of structures at the cover/basement transition can be transferred to other subsurface sites within the Upper Rhine Graben to assist the deep geothermal exploration in this promising area.

## Author contributions

Chrystel Dezayes and Catherine Lerouge designed the study, collected and analyzed the data, and wrote the paper for the structural part and the mineralogical part respectively. They lead the study and contributed to the interdisciplinary discussion. Christophe Innocent performed the U/Th analysis and their interpretation. Philippe Lach carried out ICP-MS laser analysis on quartz and participated to the writing. All authors reviewed and approved the manuscript.

## Declaration of competing interest

The authors declare that they have no known competing financial interests or personal relationships that could have appeared to influence the work reported in this paper.

## Acknowledgements

This study was co-funded by ANR (French National Research Agency) in the framework of the ANR project CANTARE-Alsace (ANR-15-CE06-0014). The authors would like to thank Jérémie De Bonneval, director of Leonhart for permitting the access of the quarry. For analytics, the authors thank Cédric Duee (BRGM) for SEM images, Nicolas Maubec (BRGM) for X-Ray diffraction on clays, and Guillaume Wille (BRGM) for electron microprobe. Patricia Bobeck is thanked for the improvement of the English language. We also thank the Editor Stephen Laubach, John Hooker, Bill Dunne, and an anonymous reviewer for constructive remarks and critical reviews that greatly improved the article.

## Appendix A. Supplementary data

Supplementary data to this article can be found online at https://doi.org/10.1016/j.jsg.2021.104323.

## References


Ackerer, J., Chabaux, F., Van der Woerd, J., Viville, D., Pelt, E., Kali, E., Lerouge, C., Ackerer, P., di Chiara Roupert, R., Négrel, P., 2016. Regolith evolution on the millennial timescale from combined U–Th–Ra isotopes and in situ cosmogenic 10Be analysis in a weathering profile (Strengbach catchment, France). Earth Planet Sci. Lett. 453, 33–43. https://doi.org/10.1016/j.epsl.2016.08.005.

Aliyu, M.D., Chen, H.-P., 2018. Enhanced geothermal system modelling with multiple pore media: thermo-hydraulic coupled processes. Energy 165, 931–948. https://doi.org/10.1016/j.energy.2018.09.129.

Allan, M.M., Yardley, B.W.D., 2007. Tracking meteoric infiltration into a magmatic-hydrothermal system: a cathodoluminescence, oxygen isotope and trace element study of quartz from Mt. Leyshon, Australia. Chem. Geol. 240, 343–360. https://doi.org/10.1016/j.chemgeo.2007.03.004.

Altherr, R., Henes-Klaiber, U., Hegner, E., Satir, M., Langer, C., 1999. Plutonism in the variscan odenwald (Germany): from subduction to collision. Int. J. Earth Sci. 88, 422–443. https://doi.org/10.1007/s005310050276.

Altherr, R., Holl, A., Hegner, E., Langer, C., Kreuzer, H., 2000. High-potassium, calcalkaline I-type plutonism in the european variscides: northern vosges (France) and northern schwarzwald (Germany). Lithos 50, 51–73. https://doi.org/10.1016/S0024-4937(99)00052-3.

Antonellini, M., Aydin, A., 1994. Effect of faulting on fluid flow in porous sandstones: petrophysical Properties 1. AAPG (Am. Assoc. Pet. Geol.) Bull. 78, 355–377.

Arthaud, F., Matte, P., 1975. Les decrochements tardi-hercyniens du sud-ouest de l'europe. Geometrie et essai de reconstitution des conditions de la deformation. Tectonophysics 25 (1–2). https://doi.org/10.1016/0040-1951(75)90014-1.

Baillieux, P., Schill, E., Edel, J.-B., Mauri, G., 2013. Localization of temperature anomalies in the Upper Rhine Graben: insights from geophysics and neotectonic activity. Int. Geol. Rev. 55, 1744–1762. https://doi.org/10.1186/s40517-014-0016-y.

Barton, C.A., Zoback, M.D., Moos, D., 1995. Fluid flow along potentially active faults in crystalline rock. Geology 23, 683–686. https://doi.org/10.1130/0091-7613(1995)023<0683.

Baumgärtner, J., Lerch, C., 2013. Geothermal 2.0: the Insheim geothermal power plant. the second generation of geothermal power plants in the upper rhine graben. In: Paper Presented at Proceedings of Third European Geothermal Review.

Bergerat, F., 1987. Paléo-champs de contraintes tertiaires dans la plateforme européenne au front de l'orogène alpin. Bull. Soc. géol. France III, 611–620. https://doi.org/10.2113/gssgfbull.III.3.611.

Bertrand, L., Jusseaume, J., Géraud, Y., Diraison, M., Damy, P.-C., Navelot, V., Haffen, S., 2018. Structural heritage, reactivation and distribution of fault and fracture network in a rifting context: case study of the western shoulder of the Upper Rhine Graben. J. Struct. Geol. 108, 243–255. https://doi.org/10.1016/j.jsg.2017.09.006.

Blaise, T., Barbarand, J., Kars, M., Ploquin, F., Aubourg, C., Brigaud, B., Cathelineau, M., El Albani, A., Gautheron, C., Izart, A., Janots, D., Michels, R., Pagel, M., Pozzi, J.P., Boiron, M.C., Landrein, P., 2014. Reconstruction of low temperature (<100 °C) burial in sedimentary basins: A comparison of geothermometer in the intracontinental Paris Basin. Mar. Petrol. Geol. 53, 71–87. https://doi.org/10.1016/j.marpetgeo.2013.08.019.

Blanalt, J., Maire, G., Cloots, A., Geissert, F., Hummel, P., Stieber, A., 1972. Notice explicative de la carte géologique de France (1/50 000), feuille Brumath-Drusenheim (234). Carte géologique de la France à 1/50 000. BRGM, p. 31. Ed.

Boutin, R., Montigny, R., Thuizat, R., 1995. Chronologie K-Ar et 39Ar/40Ar du métamorphisme et du magmatisme des Vosges. Comparaison avec les massifs varisques avoisinants. Géologie de la France 1, 3–25.

Caine, J., Forster, C., 1999. fault zone architecture and fluid flow: insights from field data and numerical modeling. In: Haneberg, W.C., Mozley, P.S., Moore, J.C., Goodwin, L. B. (Eds.), Faults and Subsurface Fluid Flow in the Shallow Crust, vol. 113. Geophysical Monographs, pp. 101–127.

Caine, J.S., Evans, J.P., Forster, C.B., 1996. Fault zone architecture and permeability structure. Geology 24, 1025–1028. https://doi.org/10.1130/0091-7613(1996)024<1025:FZAAPS>2.3.CO;2.

Callahan, O.A., Eichhubl, P., Olson, J.E., Davatzes, N.C., 2019. Fracture mechanical properties of damaged and hydrothermally altered rocks, Dixie Valley-Stillwater fault zone, Nevada, USA. J. Geophys. Res.: Solid Earth 124, 4069–4090. https://doi.org/10.1029/2018JB016708.

Callahan, O.A., Eichhubl, P., Davatzes, N.C., 2020a. Mineral precipitation as a mechanism of fault core growth. J. Struct. Geol. 140 https://doi.org/10.1016/j.jsg.2020.104156.

Callahan, O.A., Eichhubl, P., Olson, J.E., Davatzes, N.C., 2020b. Experimental investigation of chemically aided fracture growth in silicified fault rocks. Geothermics 83. https://doi.org/10.1016/j.geothermics.2019.101724.

Carasco, B., 1989. Lacustrine sedimentation in a Permian intermontane basin: the Villé graben (Vosges, France). Palaeogeogr. Palaeoclimatol. Palaeoecol. 70, 179–186.

Cardell, C., Yebra, A., Van Grieken, R., 2002. Applying Digital Image Processing to SEM-EDX and BSE Images to Determine and Quantify Porosity and Salts with Depth in Porous Media. Microchim Acta 140, 9–14. https://doi.org/10.1007/s006040200063.

Cathelineau, M., Boiron, M.-C., 2010. Downward penetration and mixing of sedimentary brines and dilute hot waters at 5km depth in the granite basement at Soultz-sous-Forêts (Rhine graben, France). Comptes Rendus Geosci., Academie des sciences 342, 560–565. http://linkinghub.elsevier.com/retrieve/pii/S1631071309002284.

Chabaux, F., Riotte, J., Dequincey, O., 2003. U-Th-Ra fractionation during weathering and river transport. Rev. Mineral. Geochem. 52, 533–576. https://doi.org/10.2113/0520533.

Crider, J.G., 2015. The initiation of brittle faults in crystalline rock. J. Struct. Geol. 77, 159–174. https://doi.org/10.1016/j.jsg.2015.05.001.

Davy, P., Darcel, C., Bour, O., Munier, R., de Dreuzy, J.R., 2006. A note on the angular correction applied to fracture intensity profiles along drill core. J. Geophys. Res. 111, B11408. https://doi.org/10.1029/2005JB004121.

Dezayes, C., Lerouge, C., 2019. Reconstructing paleofluid circulation at the hercynian basement/mesozoic sedimentary cover interface in the upper rhine graben. Geofluids 2019, 1–30. https://doi.org/10.1155/2019/4849860.

Dimmen, V., Rotevatn, A., Peacock, D.C.P., Nixon, C.W., Nærland, K., 2017. Quantifying structural controls on fluid flow: insights from carbonate-hosted fault damage zones on the Maltese Islands. J. Struct. Geol. 101, 43–57.

Drüppel, K., Stober, I., Grimmer, J.C., Mertz-Kraus, R., 2020. Experimental alteration of granitic rocks: implications for the evolution of geothermal brines in the Upper Rhine Graben, Germany. Geothermics 88, 101903. https://doi.org/10.1016/j.geothermics.2020.101903, 2020 ISSN 0375–6505.

Edel, J., Fluck, P., 1989. The upper Rhenish Shield basement (Vosges, Upper Rhinegraben and Schwarzwald): main structural features deduced from magnetic, gravimetric and geological data. Tectonophysics 169, 303–316. https://doi.org/10.1016/0040-1951(89)90093-0.

Edel, J.-B., Schulmann, K., 2009. Geophysical constraints and model of the Saxothuringian and Rhenohercynian subductions −magmatic arc system in NE France and SW Germany. Bull. Soc. Geol. Fr. 180, 545–558.

Edel, J.B., Weber, K., 1995. Cadomian terranes, wrench faulting and thrusting in the central Europe Variscides: geophysical and geological evidence. Geol. Rundsch. 84, 412–432. https://doi.org/10.1007/BF00260450.

Edel, J.-B., Schulmann, K., Rotstein, Y., 2007. The variscan tectonic inheritance of the upper rhine graben: evidence of reactivations in the lias, late eocene–oligocene up to the recent. Int. J. Earth Sci. 96, 305–325. https://doi.org/10.1007/s00531-006-0092-8.

Fleischer, R.L., 1980. Isotopic disequilibrium of uranium: alpha-recoil damage and preferential solution effects. Science 207, 979–981.

Freymark, J., Sippel, J., Scheck-Wenderoth, M., Bär, K., Stiller, M., Fritsche, J.G., Kracht, M., 2017. The deep thermal field of the Upper Rhine Graben. Tectonophysics 694, 114–129. https://doi.org/10.1016/j.tecto.2016.11.013.

Genter, A., Evans, K., Cuenot, N., Fritsch, D., Sanjuan, B., 2010. Contribution of the exploration of deep crystalline fractured reservoir of Soultz to the knowledge of enhanced geothermal systems (EGS). Compt. Rendus Geosci. 342, 502–516. https://doi.org/10.1016/j.crte.2010.01.006.

Gentier, S., Hopkins, D., Riss, J., 2000. Role of fracture geometry in the evolution of flow paths under stress. In: Dynamic of Fluids in Fractured Rock, Geophysical Monograph, vol. 122, pp. 169–183.

Gillespie, P.A., Howard, C.B., Walsh, J.J., Watterson, J., 1993. Measurement and characterisation of spatial distributions of fractures. Tectonophysics 226, 113–141. https://doi.org/10.1016/0040-1951(93)90114-Y.

Gillespie, P., Johnston, J.D., Loriga, M.A., McCaffrey, K.J.W., Walsh, J.J., Watterson, J., 1999. Influence of layering on vein systematics in line samples. In: McCaffrey, K.J. W., Lonergan, L., Wilkinson, J.J. (Eds.), Fract. Fluid Flow Miner. Geological Society Special Publication, London, pp. 35–56, 1999.

Haertel, M., Herwegh, M., Pettke, T., 2013. Titanium-in-quartz thermometry on synkinematic quartz veins in a retrograde crustal-scale normal fault zone. Tectonophysics 608, 468–481. https://doi.org/10.1016/j.tecto.2013.08.042.

Heap, M.J., Kennedy, B.M., Farquharson, J.I., Ashworth, J., Mayer, K., Letham-Brake, M., Reuschlé, T., Gilg, H.A., Scheu, B., Lavallée, Y., Siratovich, P., Cole, J., Jolly, A.D., Baud, P., Dingwell, D.B., 2017. A multidisciplinary approach to quantify the permeability of the Whakaari/White Island volcanic hydrothermal system (Taupo Volcanic Zone, New Zealand). J. Volcanol. Geoth. Res. 332, 88–108. https://doi.org/10.1016/j.jvolgeores.2016.12.004.

Hettkamp, T., Baumgärtner, J., Teza, D., Lerch, C., 2013. Experiences from 5 years operation in Landau. Reviews of geophysics. In: Paper Presented at Proceedings of Third European Geothermal.

Hollinsworth, A.D., Koehn, D., Dempster, T.J., Aanyu, K., 2019. Structural controls on the interaction between basin fluids and a rift flank fault: constraints from the Bwamba Fault, East African Rift. J. Struct. Geol. 118, 236–249. https://doi.org/10.1016/j.jsg.2018.10.012.

Hooker, J.N., Laubach, S.E., Marrett, R., 2018. Microfracture spacing distributions and the evolution of fracture patterns in sandstones. Journal of Structural Geology, Spatial Arrangement of Fractures and Faults 108, 66–79. https://doi.org/10.1016/j.jsg.2017.04.001.

Hurter, S., Schellschmidt, R., 2003. Atlas of geothermal resources in Europe. Geothermics 32, 779–787. https://doi.org/10.1016/S0375-6505(03)00070-1.

Illies, J.H., 1972. The Rhine graben rift system-plate tectonics and transform faulting. Geophys. Surv. 1, 27–60.

Illies, J., Greiner, G., 1978. Rhinegraben and the alpine system. GSA Bulletin 89, 770–782. https://doi.org/10.1130/0016-7606(1978)89<770:RATAS>2.0.CO;2.

Kratinová, Z., Schulmann, K., Edel, J.-B., Ježek, J., Schaltegger, U., 2007. Model of successive granite sheet emplacement in transtensional setting: integrated microstructural and anisotropy of magnetic susceptibility study. Tectonics 26. https://doi.org/10.1029/2006TC002035.

Kushnir, A.R.L., Heap, M.J., Baud, P., Gilg, H.A., Reuschlé, T., Lerouge, C., Dezayes, C., Duringer, P., 2018. Characterizing the physical properties of rocks from the paleozoic to permo-triassic transition in the upper rhine graben. Geoth. Energy 6, 16. https://doi.org/10.1186/s40517-018-0103-6.

Laubach, S.E., Eichhubl, P., Hargrove, P., Ellis, M.A., Hooker, J.N., 2014. Fault core and damage zone fracture attributes vary along strike owing to interaction of fracture growth, quartz accumulation, and differing sandstone composition. J. Struct. Geol. 68 (Part A), 207–226. https://doi.org/10.1016/j.jsg.2014.08.007.

Laubach, S.E., Lamarche, J., Gauthier, B.D.M., Dunne, W.M., Sanderson, D.J., 2018. Spatial arrangement of faults and opening-mode fractures. J. Struct. Geol. 108, 2–15. https://doi.org/10.1016/j.jsg.2017.08.008.

Laubach, S.E., Lander, R.H., Criscenti, L.J., et al., 2019. The role of chemistry in fracture pattern development and opportunities to advance interpretations of geological materials. Rev. Geophys. 57 (3), 1065–1111. https://doi.org/10.1029/2019RG000671.

Laubacher, G., von Eller, J.-P., 1966. Contribution à l'étude géologique des dépôts permiens du Bassin de Villé. Sciences Géologiques, bulletins et mémoires, pp. 163–186.

Le Carlier, C., Royer, J.J., Flores, E.L., 1992. Convective heat transfer at the Soultz-sous-Forêts Geothermal Site: implications for oil potential. First Break 12, 553–560.

Liewig, N., Clauer, N., 2000. K-Ar dating of varied microtextural illite in Permian gas reservoirs, northern Germany. Clay Miner. 35, 271–281.

Long, J.C., Witherspoon, P.A., 1985. The relationship of the degree of interconnection to permeability in fracture networks. J. Geophys. Res.: Solid Earth 90 (B4), 3087–3098. https://doi.org/10.1029/JB090iB04p03087.

Marrett, R., Gale, J.F.W., Gomez, L., Laubach, S.E., 2018. Correlation analysis of fracture arrangement in space. J. Struct. Geol. 108, 16–33. https://doi.org/10.1016/j.jsg.2017.06.012.

Meixner, J., Schill, E., Grimmer, J.C., Gaucher, E., Kohl, T., Klingler, P., 2016. Structural control of geothermal reservoirs in extensional tectonic settings: an example from the Upper Rhine Graben. J. Struct. Geol. 82, 1–15. https://doi.org/10.1016/j.jsg.2015.11.003.

Merlet, C., 1994. An accurate computer correction program for quantitative electron probe microanalysis. Mikrochim. Acta 114–115, 363–376.

Millot, R., Guerrot, C., Innocent, C., Négrel, P., Sanjuan, B., 2011. Chemical, multi-isotopic (Li-B-Sr-U-H-O) and thermal characterization of Triassic formation waters from the Paris Basin. Chem. Geol. 283, 226–241. https://doi.org/10.1016/j.chemgeo.2011.01.020.

Moir, H., Lunn, R.J., Shipton, Z.K., Kirkpatrick, J.D., 2010. Simulating brittle fault evolution from networks of pre-existing joints within crystalline rock. J. Struct. Geol. 32 (11), 1742–1753. https://doi.org/10.1016/j.jsg.2009.08.016.

Monnier, L., Lach, P., Salvi, S., Melleton, J., Bailly, L., Béziat, D., Monnier, Y., Gouy, S., 2018. Quartz trace-element composition by LA-ICP-MS as proxy for granite differentiation, hydrothermal episodes, and related mineralization: The Beauvoir Granite (Echassières district), France. Lithos 320-321, 355–377. https://doi.org/10.1016/j.lithos.2018.09.024.

Pearce, N.J., Perkins, W.T., Westgate, J.A., Gorton, M.P., Jackson, S.E., Neal, C.R., Chenery, S.P., 1997. A compilation of new and published major and trace element data for NIST SRM 610 and NIST SRM 612 glass reference materials. Geostandards and Geoanalytical Research 21, 115–144.

Pickering, G., Bull, J.M., Sanderson, D.J., 1995. Sampling power-law distributions. Tectonophysics 248, 1–20. https://doi.org/10.1016/0040-1951(95)00030-Q.

Pribnow, D., Schellschmidt, R., 2000. Thermal tracking of upper crustal fluid flow in the Rhine Graben. Geophysical Research Letters – Geophys. Res. Let. 27, 1957–1960. https://doi.org/10.1029/2000GL008494.

Priest, S.D., Hudson, J.A., 1981. Estimation of discontinuity spacing and trace length using scanline surveys. Int. J. Rock Mech. Min. Sci. Geomech. Abstr. 18, 183–197.

Questiaux, J.M., Couples, G.D., Ruby, N., 2010. Fractured reservoirs with fracture corridors. Geophys. Prospect. 58, 279–295. https://doi.org/10.1111/j.1365-2478.2009.00810.x.

Rauch, A., Sartori, M., Rossi, E., Baland, P., Castelltort, S., 2019. Trace Information Extraction (TIE): a new approach to extract structural information from traces in geological maps. J. Struct. Geol. 126, 286–300. https://doi.org/10.1016/j.jsg.2019.06.007.

Rotstein, Y., Edel, J.B., Gabriel, G., Boulanger, D., Schaming, M., Munschy, M., 2006. Insight into the structure of the upper rhine graben and its basement from a new compilation of bouguer gravity. Tectonophysics 425, 55–70. https://doi.org/10.1016/j.tecto.2006.07.002.

Rotevatn, A., Thorsheim, E., Bastesen, E., Fossmark, H.S.S., Torabi, A., Sælen, G., 2016. Sequential growth of deformation bands in carbonate grainstones in the hanging wall of an active growth fault: implicationsfor deformation mechanisms in different tectonic regimes. Journal of Structural Geology 90, 27–47. https://doi.org/10.1016/j.jsg.2016.07.003.

Rotstein, Y., Edel, J.-B., Gabriel, G., Boulanger, D., Schaming, M., Munschy, M., 2006. Insight into the structure of the Upper Rhine Graben and its basement from a new compilation of Bouguer Gravity. Tectonophysics 425, 55–70. https://doi.org/10.1016/j.tecto.2006.07.002.

Sanderson, D., Peacock, D., 2019. Line sampling of fracture swarms and corridors. J. Struct. Geol. 122, 27–37. https://doi.org/10.1016/j.jsg.2019.02.006.

Sanjuan, B., Millot, R., Innocent, C., Dezayes, C., Scheiber, J., Brach, M., 2016. Major geochemical characteristics of geothermal brines from the Upper Rhine Graben granitic basement with constraints on temperature and circulation. Chem. Geol. 428, 27–47. https://doi.org/10.1016/j.chemgeo.2016.02.021.

Schaffhauser, T., 2013. Tracing and Modeling of Weathering Processes on a Small Catchment Scale : the Ringelbach (Vosges, France). PhD thesis. Strasbourg University.

Schellschmidt, R., Clauser, C., 1996. The thermal regime of the upper rhine graben and the anomaly at Soultz. Z. Angew. Geol. 42, 40–44.

Schleicher, A.M., Warr, L.N., Kober, B., Laverret, E., Clauer, N., 2006. Episodic mineralization of hydrothermal illite in the soultz-sous-forêts granite (upper rhine graben, France). Contrib. Mineral. Petrol. 152, 349–364.

Schulmann, K., Schaltegger, U., Jezek, J., Thompson, A., Edel, J.B., 2002. Rapid burial and exhumation during orogeny:thickening and synconvergent exhumation of thermally weakend and thinned crust (Variscan orogen in western Europe). Am. J. Sci. 302, 856–879.

Schumacher, M.E., 2002. Upper Rhine Graben: role of preexisting structures during rift evolution. Tectonics 21. https://doi.org/10.1029/2001TC900022, 6-1-6-17.

Schweizer, V., Kraatz, R., 1982. Kraichgau und südlicher Odenwald. Slg Geol Führer 72.

Sittler, C., 1992. Illustration de l'histoire géologique du Fossé rhénan et de l'Alsace. Neues Jahrbuch Geol. Palaontol. Abhand. 186, 255–282, 1992.

Skrzypek, E., 2011. Contribution structural, pétrologique et géochronologique à la tectonique intracontinentale de la chaîne hercynienne d'Europe (Sudètes, Vosges). Phd thesis. Strasbourg University, p. 416.

Skrzypek, E., 2016. Eléments de notice pour la carte harmonisée du nord-Est de la France à l'échelle 1/50000. BRGM.

Skrzypek, E., Schulmann, K., Tabaud, A., Edel, J., 2014. Palaeozoic Evolution of the Variscan Vosges Mountains. The Variscan Orogeny, 405. Geological Society, London, pp. 45–75. https://doi.org/10.1144/SP405.8. Special Publications.

Solum, J.G., Davatzes, N.C., Lockner, D.A., 2010. Fault-related clay authigenesis along the Moab Fault; implications for calculations of fault rock composition and mechanical and hydrologic fault zone properties. J. Struct. Geol. 32 (12), 1899–1911. https://doi.org/10.1016/j.jsg.2010.07.009.

Tabaud, A., Whitechurch, H., Rossi, P., Schulmann, K., Guerrot, C., Cocherie, A., 2014. Devonian–Permian magmatic pulses in the northern Vosges Mountains (NE France): result of continuous subduction of the Rhenohercynian Ocean and Avalonian passive margin. Geol Soc Lond Special Publ 405, 197–223. https://doi.org/10.1144/SP405.12.

Taylor, S.R., McLennan, S.M., 1995. The geochemical evolution of the continental crust. Rev. Geophys. 33, 241–265.

Terzaghi, R., 1965. Sources of Error in Joint Surveys. Geotechnique, pp. 287–304. https://doi.org/10.1680/geot.1965.15.3.287.

Torabi, A., Ellingsen, T.S.S., Johannessen, M.U., Alaei, B., Rotevatn, A., Chiarella, D., 2019. Fault Zone Architecture and its Scaling Laws: where Does the Damage Zone Start and Stop?, 496 Geological Society, London, pp. 99–124. https://doi.org/10.1144/SP496-2018-151.

Ukar, E., Laubach, S.E., Hooker, J.N., 2019. Outcrops as guides to subsurface natural fractures: example from the Nikanassin Formation tight-gas sandstone, Grande Cache, Alberta Foothills, Canada. Mar. Petrol. Geol. 103, 255–275. https://doi.org/10.1016/j.marpetgeo.2019.01.039.

Valley, B.C., 2007. He Relation Betwenn Natural Fracturing and Stress Heterogeneities in Deep-Seated Crystalline Rocks at Soultz-Sous-Forêts (France). PhD thesis. ETH Zurich. n°17358.

Vallier, B., Magnenet, V., Schmittbuhl, J., Fond, C., 2019. Contribution of Large-Scale Faults on Hydrothermal Circulation in Deep Geothermal Reservoir in the Upper Rhine Graben. European Geothermal Congress 2019. Den Haag, The Netherlands, 11-14 June 2019.

Vidal, J., Genter, A., Chopin, F., 2017. Permeable fracture zones in the hard rocks of the geothermal reservoir at Rittershoffen, France. J. Geophys. Res. : Solid Earth 122, 4864–4887. https://doi.org/10.1002/2017JB014331.

Villemin, T., Bergerat, F., 1987. L'évolution structurale du fossé rhénan au cours du Cénozoïque: un bilan de la déformation et des effets thermiques de l'extension. Bull. Soc. géol. France III, 245–255.

Walter, B.F., Immenhauser, A., Geske, A., Markl, G., 2015. Exploration of hydrothermal carbonate magnesium isotope signatures as tracers for continental fluid aquifers, Schwarzwald mining district, SW Germany. Chem. Geol. 400, 87–105.

Wang, Q., Laubach, S.E., Gale, J.F.W., Ramos, M.J., 2019. Quantified fracture (joint) clustering in Archean basement, Wyoming: application of the normalized correlation count method. Petrol. Geosci. 25, 415–428. https://doi.org/10.1144/petgeo2018-146.

Wark, D.A., Watson, E.B., 2006. TitaniQ: a titanium-in-quartz geothermometer. Contrib. Mineral. Petrol. 152, 743–754.

Wedepohl, H.K., 1995. The composition of the continental crust. Geochem. Cosmochim. Acta 59, 1217–1232.

Wyns, R., 1999. Contraintes géologiques et géomorphologiques à l'histoire de la mobilité verticale de la lithosphère continentale en Europe de l'ouest depuis le Crétacé : relations avec la genèse des grabens et du volcanisme tertiaires. In: Nehlig, P. (Ed.), Colloque « Volcanismes, sédimentations et tectoniques cénozoïques périalpins ». Doc, vol. 291. BRGM, Aurillac, pp. 46–47.

Wyns, R., Baltassat, J.M., Lachassagne, P., Legchenko, A., Vairon, J., Mathieu, F., 2004. Application of SNMR soundings for groundwater reserves mapping in altered basement rocks (Brittany, France). Bull. Soc. Geol. Fr. 175, 21–34.

Ziegler, P.A., 1992. European Cenozoic rift system. Tectonophysics 208, 91–111. https://doi.org/10.1016/0040-1951(92)90338-7.

Ziegler, P.A., Dèzes, P., 2005. Evolution of the lithosphere in the area of the rhine Rift System. Int. J. Earth Sci. 94, 594–614. https://doi.org/10.1007/s00531-005-0474-3.